Pre-submission authors draft.

Hypozonal gold mineralisation in shear zone hosted deposits driven by fault valve action and fluid mixing: the Nalunaq deposit, Greenland.

Martin Smith[1*], David Banks[2], Santanu Ray[1], Francis Bowers[3#]

1 School of Environment and Technology, University of Brighton, Brighton BN2 4GJ, U.K.

2 School of Earth and Environment, University of Leeds, Leeds, LS2 9JT, U.K.

3 Angel Mining PLC., London, EC1A 2AY, U.K.

***Corresponding Author:** martin.smith@brighton.ac.uk

#Current Address: Blackwell Earthmoving Ltd, West Terrace, Esh Winning, Durham, DH7 9PT

Abstract

The Nalunaq deposit, Greenland, is a hypozonal, shear zone-hosted, Au deposit. The shear zone has previously been interpreted to have undergone 4 stages of deformation. Each stage was accompanied by fluid flow recorded by vein formation and fluid inclusion trapping. Coupled with previous trapping T estimates fluid inclusion microthermometric data are consistent with trapping of fluids with salinities between 28-45 wt. % NaCl eq., from 300-475°C during D2 and D3, with pressure varying between ~800 and 100Mpa. The range reflects pressure cycling during seismic slip related depressurisation events. D4 fluids were lower salinity and trapped from 200-300°C, at ~50-200Mpa during late stage normal faulting. The variation in major element chemistry is consistent with ingress of hypersaline granitoid equilibrated fluids into the shear zone system and mixing with fluids that had reacted with the host metamorphic rocks. D4 stage fluids represent ingress of meteoric fluids into the system. Gold contents in inclusion fluids range from ~300-10mg/kg. These data are consistent with the high P-T solubility of Au as $AuHS(H_2S)_3^0$ complexes, and Au deposition by decompression and cooling. Gold distribution was modified by the release of chemically bound or nanoscale Au during sulphide oxidation at the D4 and subsequent stages.

The classification of metamorphic rock and shear zone hosted gold deposits has developed over recent decades as understanding of genetic mechanisms and geological associations has improved (Goldfarb and Groves, 2015). Gold deposits in metamorphic terranes have now been subdivided into orogenic gold (Groves et al., 1998; Groves et al., 2003; Goldfarb and Groves, 2015), pluton or intrusion related gold (e.g. Sillitoe, 1991; Thompson et al., 1999), gold skarns developed on the margins of porphyry intrusions (e.g. Meinert, 1993; Valance et al., 2009) and hypozonal gold skarns (e.g. Kolb et al., 2015). This broad grouping of deposit types includes a wide range of structural settings (e.g. McCuaig and Kerrich, 1998, Micklethwaite and Cox, 2006), involving fluid sources including metamorphic devolatilisation (e.g. Phillips and Powell, 2010), magmatic fluids (e.g. Sillitoe, 2008) and meteoric water (e.g. Menzies et al., 2014). Gold is dominantly thought to be transported as bisulphide complexes, and the dominant gold depositional mechanism has been inferred to be reduction in H_2S content of fluids via wall rock sulphidation (Ridley et al., 1996), but also by pH increase (Hayashi and Ohmoto, 1991), ore fluid reduction or oxidation by wall rock interaction (Robb, 2005), decreasing pH as a result of potassic or carbonate alteration (Kishida and Kerrick, 1987), loss of H_2S to the gas phase as a result of aqueous-carbonic fluid immiscibility (Spooner et al., 1987) or cooling (Phillips and Powell, 1993). Coupled to this, the development of deposits in actively deforming scenarios, at various points in metamorphic P-T-t paths, means there is significant potential for overprinting of multiple fluids, reactivation of structures and redistribution of gold (e.g. Kolb et al., 2004). Groves et al., (1998) and Goldfarb and Groves (2015) pointed to globally consistent fluid compositions (low salinity (3-7wt. % NaCl eq.), aqueous-carbonic fluids with Na-K-Ca-Mg as the dominant cations with CO_2, CH_4, N_2 and H_2S in the gas phase) as indicating orogenic gold deposits as a class clearly distinct from others, despite a wide range of formation conditions (180-700°C; 1-3kbar). Recent experiments have also increased knowledge of the range and stoichiometry of complex ions which may be involved in gold transport in hydrothermal systems, most commonly including bisulphide and chloride (e.g. Seward et al., 1973; Gammons et al., 1997; Frank et al., 2002; Williams-Jones et al., 2009; Guo et al.,

2018), and more stoichiometrically complex ions at high pressure and temperature (e.g. $AuHS(H_2S)_3^0$; Louks and Mavrogenes, 1999). The use of laser ablation ICP-MS for fluid inclusion analyses has provided direct evidence of gold concentrations in natural and experimental fluids (e.g. Heinrich et al., 1999; 2003; Simon et al., 2005; Rauchstein-Martinek et al., 2014). The role of colloidal and nanoscale particles in gold transport at concentrations above those predicted from solubility experiments has been noted by Williams-Jones et al., (2009) and demonstrated in inclusions of metamorphic fluids from the Kola superdeep borehole (Prokofiev et al., 2020) and in epithermal fluids (Banks et al., 2018).

The Nalunaq shear zone hosted gold deposit, Greenland (Kaltoft et al., 2000; Schlatter and Olsen, 2011), provides an ideal site to investigate the relative contribution of different fluid sources, deposition mechanisms, the transport of Au and the role of syn- and post-depositional processes in the formation of an upper greenschist to lower amphibolite facies, shear zone-hosted system (Bell et al., 2017a, b). The deposit has been classified as an orogenic gold deposit, but the high T, skarn-like alteration assemblage (Kaltoft et al., 2000; Bell et al., 2017a) and the high salinity of fluid inclusions (Kaltoft et al., 2000) have been used to infer magmatic fluid input. Here we present a fluid inclusion microthermometric and laser ablation ICP-MS study of fluid inclusion chemistry, supplemented with X-ray photoelectron spectroscopy (XPS) used to define the distribution and chemical state of gold associated with sulphides and quartz. These data are used to investigate the origin of vein forming fluids, the fluid pressure history of the deposit and the origin of the highly variable gold grade throughout the deposit.

GEOLOGY

The Nalunaq mine is situated on the Nanortalik peninsula, south Greenland (Fig. 1; Kaltoft et al., 2000; Bell et al., 2017a, b). The mine operated from 2004 to 2014 (Schlatter and Olsen, 2011; Bell et al., 2017a) producing 10.67tonnes (t) of gold from 713,000t of ore, with an average grade of 15g/t (Bell et al., 2017a). The grade of the deposit is very variable within the main vein, ranging from zones with <1g/t, an ore zone

that may typically grade several 100g/t and maximum reported grades of 5200g/t over a 0.8m borehole intersection (Schlatter and Olsen, 2011). Gold is typically coarse (over 30% of grains >100μm), with a strong nugget effect on grade distribution, and dominantly present as native Au, with minor maldonite (Au_2Bi; Dominy and Petersen, 2005). The Main Vein, which hosts the majority of the ore, varies between 0.05 to 1.6m thick, and dips 34-36°SE (Bell et al., 2017b).

The Nalunaq deposit is Palaeoproterozic in age (Bell et al 2017a) and is hosted by Ketilidian mobile belt rocks formed between 1850-1750Ma. The deposition of the host metavolcanic and metasedimentary rock sequence and subsequent intrusions have been related to the formation of the Nuna/Columbia supercontinent (Garde et al. 2002) and are interpreted to represent forearc sediments and volcanic rocks (Chadwick and Garde 1996). Nalunaq lies in the Southern Domain of the Ketilidian orogeny, near the contact with the Central Domain rocks of the Julianhåb igneous complex (Bell et al., 2017a,b). The overall structure of the site is part of the Nanortalik Nappe, and the host sequence is intruded by rocks of the Ilua plutonic suite (Petersen and Olsen, 1995). The general stratigraphy of the area includes meta-arkose, silicified siltstone with pyrite and graphitic layers (Schlatter and Olsen, 2011), and layers of calcareous metasediment overlain by fine grained amphibolite and with coarser grained dolerite sills (Bell et al., 2017a). The amphibolites contain minor amounts of pyrite, pyrrhotite, ilmenite and some chalcopyrite (Schlatter and Olsen, 2011; Bell et al., 2017a).

Four deformation stages have been identified in the mine area by Bell et al (2017a, b), and correlated with regional deformation stages (e.g. Garde et al, 2002). The first deformation stage (D1) consists of SE dipping foliation formed during prograde metamorphism to amphibolite facies. This is cut by reverse sense shear zones (D2) dipping SE, oblique to S1, formed under brittle-ductile conditions at lower amphibolite to upper greenschist facies conditions. The shear zone was reactivated with normal movement sense (D3) under upper greenschist facies conditions, and is in turn cut by D4 late stage faults that are inferred to be contemporaneous with the intrusion of the Ilua plutonic suite. The D2 shear zones

host the Main Vein, which is ~2km in lateral extent, mainly hosted in metabasic rocks. Quartz veins are discontinuous along the Main Vein shear zone, showing pinch and swell structures, sheeted internal morphology and either faulting/boudinage or infill of dilational jogs (Goddard, 2009). Petersen (1993) related high gold grades to dilation of voids in either drag-fold hinges, or at flexures along shear planes corresponding to changes in host rock lithology (Bell et al., 2017a, b). The main vein is cross-cut by quartz-plagioclase veins which are perpendicular to the main vein, and are inferred to be contemporaneous with main vein formation, during continuous deformation from D2 to D3 times. Gold is mainly hosted by quartz-calcite-sulphide (pyrite-arsenopyrite-pyrrhotite) veins formed during the D3 extension. Later, barren or low grade quartz veins cut the main vein and are related to the late stage fault events (Bell et al., 2017a,b) which subdivide the deposit into the Upper Block, Target Block and Southern Block (Kaltoft et al., 2000; Schlatter and Olsen, 2011).

Hydrothermal alteration associated with the vein forming events begins with calc-silicate alteration (clinopyroxene-plagioclase-garnet with minor chalcopyrite-pyrite-sphalerite-titanite), replacing the original hornblende-plagioclase assemblage (Bell et al., 2017b). Gold mineralisation is mainly hosted by the second stage of vein formation (D3) and is associated with potassic (biotite-arsenopyrite) alteration of the wall rocks, which also generated minor amounts of chlorite and sericite (Bell et al., 2017a). Uranium–Pb ages from titanite constrain the age of gold–quartz vein formation to 1783±9 to 1766±9Ma (Bell et al., 2017a, b) during retrograde exhumation of the shear zone from upper amphibolite to lower greenschist facies. This is in turn overprinted by calcite-titanite alteration associated with aplite dykes, and epidote-calcite-zoisite alteration associated with D4 faulting and biotite granodiorite intrusion, which gave U-Pb titanite ages of 1746±7Ma (Bell et al., 2017b). Igneous rocks within the Nalunaq area include aplite, calc-alkaline biotite granite and pegmatite. The aplite is tonalitic in composition, whilst the pegmatites are granodiorite to monzogranite, and the biotite granite is granite *sensu-stricto* (Schlatter and Olsen, 2011). The granite is silicified in places, with elevated Au contents, up to 200ppb. Uranium-Pb

dating of zircon by Bell et al. (2017b) indicates aplite intrusion at 1770±22Ma (contemporaneous with D2-3), pegmatite intrusion at 1747±4Ma, biotite granite intrusion at 1749±6Ma and alteration at 1742±12Ma.

Schlatter and Olsen (2011) suggested the deposits could be classified as a hypozonal orogenic gold deposit (Kolb et al., 2015), and inferred pressure–temperature conditions of 375–550°C and 200–400MPa based on the alteration mineral assemblage and the replacement of löllingite by arsenopyrite (Kaltoft et al., 2000). Preliminary fluid inclusion studies by Kaltoft et al. (2000) on quartz and clinopyroxene from mineralised and non-mineralized veins indicate aqueous (Lw+V), carbonic (CO_2-CH_4, Lc+V) and aqueous-carbonic, mainly two-phase (Lw+V) inclusions. The salinity in inclusions from non-mineralized veins was lower (4–8 wt% NaCl equiv.) or higher (31–35 wt% NaCl equiv.) than the salinity in the gold-quartz veins (14–26 wt% NaCl equiv.), with liquid vapour homogenisation temperatures (T_hL-V) in the range 150-250°C. No significant differences in CO_2-CH_4 fluid composition were noted (Kaltoft et al., 2000). Temperatures determined from arsenopyrite geochemistry showed 2 main ranges, 539-611°C and 300-475°C, implying trapping pressures for fluid inclusions of ~300MPa (~11km depth under lithostatic pressure).

METHODOLOGY

Vein samples were collected in 2 transects across the 300 and 350m levels of the Target Block (Bell et al., 2017b), Nalunaq mine (Fig. 2). Fully oriented sampling was not possible due to constraints on sampling time, but the orientation of veins relative to the strike of the main shear zone was noted, and sections were cut in reference to the strike of individual vein sections (Fig. 3). All samples were described in hand specimen and then doubly polished demountable (DPDM) wafers were viewed in transmitted and reflected light in order to constrain the paragenetic sequence of veins and contained fractures. Polished thin sections for scanning electron microscopy (SEM) were prepared from the facing surfaces of the quartz blanks used for DPDM wafer preparation. Fluid inclusion populations were defined by host vein type, cross-cutting relationships, and by the orientation of the host fractures. Within each vein type and

structural setting fluid inclusions were classified by room temperature phase assemblage (Lw - liquid water; Lc - liquid carbonic phase CO_2, CH_4; Sh - solid halite; nS - other solid phases; V - vapour). Additional SEM examination of samples was carried out in back scatter mode using a Zeiss EVO LS 15 SEM equipped with an Oxford Instruments XMax 80 EDX spectrometer at the University of Brighton using an accelerating voltage of 10kV and a beam current of 10nA.

Microthermometric data on fluid inclusions were collected using a Linkam THMSG 600 heating and freezing stage which was calibrated at -56.6°C, 0°C, and 10°C using synthetic fluid inclusion standards and distilled water, and at high temperatures using a range of pure solids. Reported temperature measurements have a precision of ±0.2°C on cooling runs, and for heating runs within ± 1°C. All measurements were made during heating runs to avoid problems of metastability. At low temperatures (<30°C) heating rates of 0.5°C/min were used, and rates of 5°C/min were used for measurements of solid dissolution and liquid-vapour homogenisation temperature (T_hL-V). Fluid inclusion salinities were calculated as weight % NaCl equivalent (wt. % NaCl eq.) directly from halite dissolution using the equation of Sterner et al. (1988) and from ice melting temperatures using the equation of Bodnar (1993). Weight % NaCl equivalent salinities were used for all inclusions to facilitate comparisons, but for Lw+V inclusions with clearly observable hydrohalite melting temperatures, total salinities in the system NaCl-$CaCl_2$-H_2O ratios are likely to be slightly higher (Oakes et al., 1990). The bulk density of inclusions was calculated from the BULK program (Bakker, 2003) using the Archer (1992) ion interaction model and data from Bodnar (1993). Isochors for all inclusions were calculated using the ISOC program (Bakker, 2003) and the equation of state for the NaCl-H_2O system of Zhang & Frantz (1987). Calculations of pressure at homogenisation and isochors for Lw+Sh+V inclusions that homogenised by halite dissolution after T_hL-V were carried out using the data of Becker et al., (2008) and Lecumberri-Sanchez et al., (2012).

Fluid inclusions were analysed following the method of Allan et al. (2005) using a GeoLas Q Plus Excimer laser (ArF, 193 nm, Microlas, Göttingen, Germany). Ablated material was transported from a

cylindrical chamber with a height of 5 mm and internal diameter of 57 mm (approximately 13 cm^3) in 0.68 L/min He via Teflon tubing to a cyclone gas mixer, where the analyte was premixed with 0.95 L/min Ar before introduction into the plasma. The analyte was analysed with an Agilent 7500c quadrupole ICP-MS, equipped with an octopole reaction cell that was pressurised with 2.5 mL/min H_2, which virtually eliminated $^{40}Ar^+$ and $^{40}Ar^{16}O^+$ interferences on $^{40}Ca^+$ and $^{56}Fe^+$, respectively, and greatly reduced the high Ar-based backgrounds on $^{39}K^+$. Fluid inclusion analyses were calibrated using combinations of NIST SRM 610 and 612, an in-house EMPA glass standard, and HNO_3 spiked aqueous standards ablated directly through the walls of glass capillaries (Gunther et al., 1997; Boue-Bigne et al., 1999). Silicate glass standards were ablated for 200 pulses over a single 50 μm spot, using a repetition rate of 5 Hz and laser fluence of 10 J/cm^2. Laser focus on the ablation surface was maintained by raising the ablation cell 1 μm per 10 shots, in accordance with an approximate ablation rate of 0.1 μm/pulse. Sodium was used as the internal standard in all cases. Sets of fluid inclusion analyses were bracketed by standards, and linear drift corrections were applied. Dwell times were 5–15 ms. Analyses of the host quartz were carried out using the same conditions on apparently solid and inclusion free areas, but with a 30μm beam diameter.

The absolute concentration of cations in analysed inclusions, and in bulk leachates was calculated by charge balance of the total cations against a Cl molality determined from microthermometric data (Allan et al., 2005). Analyses for gold were conducted with a reduced element list in order to maximise dwell time and sensitivity on the ^{197}Au peak, limiting the major elements analysed. For these analyses, data were normalised using the total Na+Ca cations, as these dominate the cation load of the fluids, charge balanced against Cl molality. Limits of determination varied according to inclusion, and were defined as 3σ in the background counts. Signals below this limit were rejected. The data for Au analyses in fluid inclusions were further filtered by examination of the time resolved laser ablation signal in order to remove analyses where Au was resolved independently of the main Na and Ca peaks, implying contamination from solid inclusions either pre- or post-breach of the fluid inclusion.

X-ray photoelectron spectroscopy (XPS) was carried out at the University of Brighton using an ESCALAB 250Xi XPS (Thermo Scientific, UK) with MAGCIS^{TM} Dual Beam Ion Source. Effective attenuation length (EAL) for XPS using the conditions here are about 10nm. XPS analysis was carried out using selected area analysis mode with a nominal width of analysis of 200 μm and monochromated Al Kα X-rays at 1486.6 eV. The MAGCIS source can generate both traditional monatomic ion beams for profiling inorganic materials and also cluster ions for organic layer profiling. In this case the gun was selected in monoatomic mode with 3 keV ion energy and raster size 0.7mm. Sputtering cycle was kept at 180 s each time with 3 cycles collected. The charge neutraliser and X-ray source were only used during the acquisition of spectra, both being turned off during the sputtering cycle. Survey (wide) scans (step size 1 eV, pass energy 150 eV, dwell time 50ms, number of scans 15) were acquired from quartz, goethite and arsenopyrite, and narrow scans (step size 0.1 eV, pass energy 20 eV, dwell time 100 ms, number of scans 25) of the Fe 2p (binding energy, BE ~ 708 eV), As 3d (~42 eV), C1s (~285 eV), O1s (~531 eV), S2p (~162 eV), Cu2p (~942 eV) and Au 4f (~88 eV) regions were acquired from arsenopyrite and goethite. Data analyses were carried out using Thermo Avantage software version 5.952. Chemical peak shift due to the sample charging under X-rays and corresponding charge neutralisation, was calculated using C1s hydrocarbon peak at 285.0 eV following standard practice. However, during sputtering, where carbon was not present, the metallic Fe 2p binding energy of 707.9 eV was used as a reference point. There is a possibility that redox reactions could be induced in the sample as it is sputtered with a monoatomic argon beam for depth profiling. In a previous study this was assessed by analysing a powder sample of reagent grade hydrated ferric sulphate ($Fe_2(SO_4)_3 \cdot 2H_2O$) was first dried at 55 °C, and then analysed to check for iron and sulphur reduction on argon ion sputtering. No effects on the XPS spectra were observed during this process (Smith et al., 2019).

RESULTS

Vein and fluid inclusion petrography.

Eight samples were collected from the 300 and 350m level stopes. The samples were selected to provide a transect across the main vein, and to include high (18 to >200g/t) and low (<1g/t) gold grades. Petrographic images of vein textures are shown in Figure 3 and 4. All samples were dominated by quartz, but show textural evidence for multiple stages of vein opening and quartz deposition. This includes strike and vein margin parallel fractures indicative of crack-seal growth in most samples. Most fractures sets are developed as conjugate pairs, although the conjugate fractures may not be as strongly developed in one orientation. Using orientation, mineralogy and cross-cutting relationships the vein and fracture generations were correlated to deformation stages identified by Bell et al., (2017a, b). The mineral paragenetic sequence and the relationship of sub-veins are shown in Figure 5. The earliest quartz generation relates to the formation of the main veins (D2) (Fig. 3) and also contains minor amounts of plagioclase feldspar and clinopyroxene (diopside). Wall rock fragments occur within the vein, and contain plagioclase, actinolite, titanite, biotite and chlorite, whilst trace amounts of K-feldspar are included in quartz (Fig. 4 A-C). This quartz is cut by quartz-plagioclase veins (Fig. 3D) in a conjugate set at high angle to the main vein. The plagioclase-quartz veining is accompanied by minor amounts of end-member albite, epidote and very minor U-Th oxides (Fig. 4D). Secondary inclusion trails sub-parallel to the plagioclase-quartz veins also occur. Both the main vein quartz and the quartz-plagioclase veins are cut by quartz-sulphide-carbonate veins (Fig. 3c, e, f) containing quartz and calcite, with minor amounts of titanite, epidote, chlorite, chalcopyrite, pyrite, arsenopyrite, pyrrhotite (Fig. 4e, f, g) and visible gold (Fig. 5a). Gold is associated with inclusions of a bismuth phase and minor amounts of maldonite (Fig. 4h). These veins and associated sub-parallel fluid inclusion trails have been linked to D3 stage extension by Bell et al., (2017a, b; Fig. 6). Relatively clear quartz is cut by conjugate fractures marked by secondary inclusion trails in most samples. These fractures formed in a brittle extensional regime and are correlated with the D4 normal faulting stage (Bell et al., 2017a, b) which is linked to alteration of the sulphide assemblage to

hydrous iron oxides. Hematite-goethite rims on arsenopyrite have been noted with Au occurring within the oxide zone (Fig. 5b, c).

Fluid inclusions were observed in all samples and images of inclusion types are shown in Figure 7. The dominant room temperature phase assemblages are aqueous liquid (Lw) plus solid halite (Sh) plus vapour (V), or with multiple solid phases (nS), and aqueous liquid plus vapour (Lw+V). The occurrence of fluid inclusions in specific structural settings is summarised in Figure 6, and illustrated in Figure 8. No unequivocally primary fluid inclusions have been observed. The inferred earliest inclusions occur in diffuse trails restricted to individual quartz grains within main vein quartz, and have Lw+nS+V or Lw+Sh+V phase assemblages (Fig. 8a). These are cut by the quartz-plagioclase veins which host similar inclusions, and are linked to linear secondary fluid inclusion trails, which cut individual grains, but not grain boundaries (and hence are inferred to pre-date D3 reactivation) hosting Lw+Sh+V and Lw+V inclusions (Fig. 8b). These are cut by the D3 quartz-sulphide carbonate veins which either host Lw+V inclusions, or have parallel fluid inclusion trails cutting multiple grains (Fig. 8C). The final stage of fluid inclusion entrapment is highly planar, conjugate fluid inclusion trails containing Lw+V inclusions, inferred to be related to the D4 normal faulting (Fig. 8c). No observations have been made in this study of carbonic and aqueous-carbonic fluid inclusions noted by Kaltoft et al. (2000). Vapour-rich inclusions were observed, but these failed to nucleate an additional vapour bubble following cooling to -120°C and presumably represent decrepitated examples of other inclusion types. Individual inclusion types were not usually developed on discrete fracture sets – i.e. Lw+Sh+V inclusions were almost always accompanied by Lw+V inclusions on the same secondary trails. This implies that the two inclusion types were probably trapped during the same or related events and that changes in salinity and homogenisation temperature may relate to continuous evolution of fluid chemistry and P-T conditions during repeated vein opening events.

Fluid inclusion microthermometry.

The results of microthermometric analyses of fluid inclusions are summarised in Table 1, and Figure 9, which also records the grade associated with bulk samples in the area of the quartz samples. The full dataset is available as Supplementary Table 1. Fluid inclusion populations were identified from the salinity and T_hL-V data, and linked to Lw+nS+V, Lw+Sh+V and Lw+V room temperature phase assemblages. Mixed fluid populations are present in most, but not all samples, and the populations are described individually below:

Population A: Lw+Sh+V and Lw+nS+V inclusions in which L-V to L homogenisation took place prior to halite dissolution. Such inclusions are complicated in interpretation as existing empirical equations for salinity determination (Sterner et al., 1988) assume the presence of the assemblage Lw+Sh+V at the final halite dissolution temperature. L-V homogenisation prior to halite dissolution means that the assemblage at dissolution is Lw+Sh, and that the inclusion internal pressure has been raised above the L+V curve for the solution when halite finally dissolves. These inclusions therefore confirm pressures of several tens to hundreds of MPa (several hundred bars to kilobars) at halite dissolution, and hence high pressures at trapping (Bodnar et al., 1994; Becker et al., 2008). These inclusions were not frozen prior to heating to preserve inclusion integrity, so only weight % NaCl equivalent salinities and homogenisation temperatures are quoted in Table 1. The population is clearly defined in Figure 9, with salinities ranging from 32 to 44 wt. % NaCl eq. and L-V homogenisation temperature ranging from 130 to 380°C. There is a broad correlation between salinity and homogenisation temperature for this population. The population is the only one occurring in Sample 1, a low-grade sample, suggesting that it is not associated with significant gold deposition.

Population B: Lw+Sh+V inclusions in which L-V homogenisation took place following halite dissolution. Salinities in these inclusions range from 28 to 32 wt. % NaCl eq. (Fig. 9). L-V homogenisation to the liquid phase characteristically occurred over a wide temperature range in these inclusions (130 to 250°C, Fig. 9)

giving rise to a clear vertical trend on a plot of salinity against T_h. This population is associated with some of the highest gold grades. In sample 3 Lw+Sh+V inclusions occur on the same trails as Lw+V inclusions (Population C) in some examples. In these inclusions halite formed from the breakdown of hydrohalite during heating following cooling to -100°C. In these cases, the inclusions must have been halite supersaturated in a metastable state during initial observation.

Population C: Lw+V inclusions which nucleate hydrohalite on cooling, and have either exceptionally low ice melting temperatures, or in which halite forms on the melting of hydrohalite and then dissolves below 100°C. First ice melting temperatures in the inclusions are typically below -50°C and may be below -60°C. The eutectic temperature for the system NaCl-$CaCl_2$-H_2O is -52.5°C, and so these low first melting temperatures indicate high concentrations of Ca and potentially other divalent cations (Fe, Mg) or Li. The combination of low ice melting and hydrohalite melting temperatures in many of these inclusions is consistent with high Ca concentrations relative to Na (Oakes et al., 1990), but salinities have been presented as NaCl equivalents here for ease of comparison with other samples. Bulk salinities of these inclusions range from 18 to 28 wt. % NaCl eq., and homogenisation temperatures from ~130 to 250°C. As with population B, these inclusions are associated with high gold grades.

Population D: Lw+V inclusions with high ice melting temperatures. First ice melting temperatures in these inclusions are typically higher than -50ºC, and in cases as high as -20ºC, essentially indicating an NaCl dominated fluid, with minor amounts of other cations, possible including KCl. Bulk salinities range from 0 to ~12 wt. % NaCl eq., and homogenisation temperatures from ~140 to 210°C. There is a clear distinction in salinity between these fluids and all others identified (Fig. 9), and this is the only population to occur in low grade samples 6 and 8, indicating it is not associated with significant gold deposition.

In terms of the relationship of fluid inclusions to the deformation history defined by Bell et al., (2017a, b) Population B is dominantly found in main vein quartz in diffuse trails linked to individual quartz veins and

so is likely the earliest population observed. Population A occurs in similar settings, and in the cross-cutting quartz-feldspar veinlets, so was trapped after Population B. Both formed during the evolution of the D2 reverse shearing event. Population C occurs in secondary trails cutting multiple grains, and in quartz-carbonate-sulphide veins, and is linked to the D3 extensional reactivation of the shear zone. Population D occurs as secondary trails in multiple samples. The highest salinity inclusions (5-15 wt. % NaCl eq.) occur in the quartz-carbonate-sulphide veins and relate to the D3 event, whilst the lowest salinity inclusions are restricted to the late stage brittle conjugate inclusion trails linked to the D4 normal faulting.

LA-ICPMS analyses of fluid inclusions.

The results of LA-ICPMS analyses of fluid inclusions are summarised in Table 2. The full data set is available in Supplementary Tables 2 and 3. Gold analyses were quality controlled using the time resolved spectra of each ablation, whereby surface contamination and Au inclusions intersected before or after the breaching of fluid inclusions could be rejected as not reflecting fluid chemistry at trapping (Fig. 10). Figure 10 also shows XPS spectra of the quartz surface. In each case the Au 4d5/2 peak is most prominent at 0 seconds, prior to sputtering with the Ar^+ ion beam, although the Au peak is resolvable in subsequent spectra. This is consistent with the distribution of Au contamination on the sample surface during polishing and sample preparation. Gold below the sample surface is present as sub-micron to nano-scale metallic inclusions clearly visible in time resolved spectra from quartz. Bulk quartz analyses were not quantified for this reason. Both were filtered from the fluid inclusion analyses using the time resolved LA-ICPMS spectra. The results of fluid inclusion analyses are shown in Figures 11, 12 and 13.

In all cases the fluids are Na-Ca-K-Fe-Mg chloride dominated, although there is some variation between Na and Ca as the dominant cation (Table 2). Calcium is the dominant cation mainly in the hypersaline brine inclusions (32-45wt. % NaCl eq.) that are inferred to be the latest stage D2 fluids. For all

fluid inclusions the relative Na-K-Mg concentrations are shown in Figure 11, compared to temperature contours based on the Na/K ratio from Can (2002), and K/√Mg ratio from Giggenbach (1988), and with the fields for immature, partially equilibrated and equilibrated waters from Giggenbach (1988). Use of these geothermometers in this context is indicative of conditions only as they are extrapolated outside of their conditions of calibration in terms of both salinity and trapping temperature. However, in nearly all cases the fluids trapped in Nalunaq quartz exceed the Mg contents expected for equilibration with K-feldspar-muscovite-chlorite-albite assemblages (Fig. 11a). Application of the revised solution Na/K geothermometer of Can (2002) is shown in Figure 11b. This implies that the D2 fluids from the main vein and quartz-plagioclase veins (samples 1, 2 and 4) equilibrated with a 2 feldspar assemblage from 300-400°C either in the source region or during hydrothermal alteration. These T estimates are at the limits of applicability of the geothermometer but are geologically reasonable, showing agreement with previous estimates from arsenopyrite composition (300-475°C; Kaltoft et al., 2000) The fluids from D3-4 stage quartz can be inferred to have equilibrated with a 2 feldspar assemblage from 200-350°C, and are the most reliable T estimates from these analyses. The remainder of samples show a high K content relative to Na (Fig, 11b), outside the range calibrated by Can (2002) and indicative of high temperature (>400°C), disequilibrium with 2 feldspar assemblages, or both. The high relative K content is most marked for fluid inclusions samples 5 and 6, which are inferred to have been trapped at very different paragenetic stages (sample 5 D2; sample 6 D4) so disequilibrium with a 2 feldspar source rock is the most likely explanation (although Kaltoft et al., (2000) noted arsenopyrite compositions consistent with temperatures as high as 539-611°C).

The major cation chemistry of the fluids is further examined in Figure 12. Dilution of initially hypersaline brines can be clearly identified from the microthermometric data, and so ratio plots are used alongside plots of reconstructed concentration in order to separate dilution from other effects. As already noted, the Na/K ratio is temperature sensitive if equilibrium with 2 feldspars is assumed. Figure 12a plots

the Na/K ratio against the Na/Ca ratio. In these samples quartz formed at a similar paragenetic stage and with similar Na/K ratio in fluid inclusions (samples 1 and 2) show very different relative levels of Ca enrichment (Fig, 12a), with remainder of samples falling between the 2 extremes of Na-rich and Ca-rich brines, coupled with overall dilution (Figure 12b). This difference is also clearly apparent in plots of Ca/Sr ratio, where Ca enrichment does not correlate with Sr enrichment, and high Ca/Sr ratios are present in the lowest Na/K ratio fluids (i.e. those potentially in disequilibrium with the host rock mineral assemblage; Fig. 12c, d), with evidence for mixing between 2 fluid compositions coupled with overall dilution. Potassium enrichment is positively correlated with Sr-enrichment (Fig. 12e). Of the major elements Fe is likely to show contrasting behaviour to the alkali and alkaline earth metals because of its redox sensitivity. Figure 12f shows a plot of Fe/Cl ratio (to account for the effects of chlorinity on Fe concentration; Kwak et al., 1986; Yardley, 2005) against Fe/Mn ratio. The Fe/Mn ratio gives an indication of the influence of redox variation due to the opposing solubility of Fe and Mn at low and high redox conditions. Iron contents are high relative to Mn in the relatively Na-rich fluids from samples 1 and 4, and less Fe-enriched in the Ca-rich samples (sample 2). Manganese was below detection limits in most other samples.

The concentrations of transition metals, including Fe are shown in Figure 13. Fe shows a strong correlation with salinity, which can be strongly linked to the control of Fe-Cl complexes on Fe solubility (Kwak et al., 1986; Yardley, 2005), with trends at high Fe content in samples 1, 4 and 5, potentially linked to more reduced fluids or source rocks, and hence a greater prevalence of Fe^{2+} (Fig. 13a). Zinc shows a similar strong dependence on chlorinity linked to transport as Zn-Cl complex ions, and Pb correlates strongly with Zn, consistent with the control of both by the solubility of sphalerite and galena (Yardley, 2005). Gold concentrations could be reliably reconstructed from just 15 analyses, but these are from across the salinity range. At high salinity in D2-3 stage fluids measurable Au concentrations range from ~25-300mg/kg, whilst in low salinity D4 fluids concentrations range from ~12-80mg/kg (Fig. 13d). Although there is broad correlation of Au with overall solution concentration, this breaks down at high

salinity suggesting Au transport was not directly related to chloride concentration. It should be noted that because of the small analyte volume in fluid inclusions, the detection limits are correspondingly higher than for bulk solution analyses, and so these analyses represent the maximum Au concentrations in solution at any given stage of the mineralising system.

XPS analyses of sulphides.

X-ray photoelectron spectra were obtained from arsenopyrite in Sample 3, and from Au-bearing goethite-hematite rims on arsenopyrite. Survey scans of arsenopyrite show the As 3p3/2 peaks at ~141eV and 144eV that can be linked to the presence of arsenide (As^{-1}, 140.5eV; Hollinger et al., 1974) and arsenate (As^{+5}, 144.3eV; Stec et al., 1972), indicating the partial oxidation of arsenopyrite. Narrow scans of the Fe 3p3/2, As 3d and Au 4f peaks from goethite on the margin of arsenopyrite are shown in Figure 14. The Fe peak can be resolved into hematite (Fe_2O_3, 711.6eV; Mills and Sullivan, 1983), iron (II) oxide (FeO, 710.7eV; Mills and Sullivan, 1983), $Fe_2(SO4)_3$ (168eV; Yu et al., 1990), grain boundary neutral Fe (708.70eV; Siriwardene et al., 1985) and metallic Fe (706.8eV; Marcus et al., 1992). All are indicative of the partial oxidation of Fe from arsenopyrite. The As 3d peak can be resolved into the As3d3/2 and As3d5/2 spin coupling states characteristic of arsenite (As^{3+}; Nesbitt and Reinke, 1999). The Au4f5/2 peak (88.1eV; Kitagawa et al., 1991) can be resolved as a shoulder on the margin of the much large Fe 3s peak at 91eV (Huntley et al., 1986), alongside the Au4f7/2 peak at 84eV (Seah et al., 1990).

DISCUSSION.

Conditions of fluid flow and mineralisation

The earliest fluids in the Nalunaq veins system are inferred to be the population A and B inclusions. Population A (salinity 32-45wt. % NaCl eq.) occurs in the extensional quartz feldspar veins which are synchronous to slightly crosscutting the main veins, so these inclusions are inferred to postdate the

population B inclusions. The population A and B inclusions typically homogenise by halite dissolution at temperatures in excess of the liquid-vapour homogenisation temperature, and so must either represent heterogeneous trapping of suspended halite particles (Becker et al., 2008), or trapping under high pressure conditions (Bodnar, 1994; Becker et al., 2008; Lecumberri-Sanchez et al., 2012). The latter is most likely here because of the consistent salinity ranges which suggest trapping of a homogeneous composition fluid, most notable for population B (28-32 wt. % NaCl eq.). The P at T_h calculated on the basis of the data and equations of Becker et al. (2008) and Lecumberri-Sanchez et al., (2012) is shown in Figure 15a, and varies between ~100 and 300MPa for inclusion that homogenise by halite disappearance, and 0.4 and 1MPa for fluid inclusions that homogenise by vapour disappearance. The calculated isochores for these populations are shown in Figure 15b. For the dominant range in T indicated by arsenopyrite geochemistry and the Na-K ratios of fluid inclusions (300-475°C) this implies trapping of the population B inclusions from ~200-900MPa, and the Population A inclusions from ~200-700MPa. Higher temperature trapping for the population B inclusions (539-611°C from arsenopyrite geochemistry) would suggest the minimum P was ~500MPa. These inferred conditions are consistent with the Upper Greenschist to Amphibolite facies conditions of shear zone activity inferred by Kaltoft et al. (2000), Dominy and Petersen (2005) and Bell et al., (2017a). If the wide range in fluid inclusion homogenisation temperature is not due to post trapping modification of fluid inclusions (leakage) then this implies that these two inclusion populations were trapped over a pressure range of 300-500MPa (3-5Kbars). Such large pressure variations are consistent with a fault-valve mechanism for vein growth and fluid flow (Sibson et al., 1988), where by fluid pressure builds up within a fracture zone until it reaches the lithostatic pressure when a fault movement occurs (a seismic event) resulting in vein dilation and the generation of permeability. The stress reduction on failure also results in the discharge of fluids from surrounding pore space into the open vein resulting in quartz (and potentially other mineral) precipitation which seals the permeability, resulting in an increase in fluid pressure. Kaltoft et al., (2000) noted the presence of CO_2-dominated carbonic

inclusions associated with halite-bearing inclusions with salinities up to 26 wt. % NaCl eq., but these have not been observed in this study. It may be that such inclusions are specifically associated with skarn zones, and if aqueous-carbonic fluid immiscibility did occur in these areas under the inferred P-T-salinity conditions, then the carbonic phase will have removed a significant amount of water from the aqueous dominant phase (Bowers and Helgeson, 1983). This may be a route for the evolution to higher salinity seen between Population B and Population A. The limits of the fluid pressures inferred, if they represent lithostatic fluid pressure post-rupture, would be consistent with the initial shear zone formation at ~11-19km depth, with super-lithostatic fluid pressures generated between rupture periods.

Population C ranges in salinity from ~28wt. % NaCl to ~15 wt. % NaCl, with a similar range in T_hL-V to Population B. The fluid inclusions are not halite saturated, because of a high Ca-content in the fluids (Oakes et al., 1990). Hydrohalite melting observed in some inclusions at around -15°C implies NaCl dominant fluids, whilst $T_m$hh between -30 to -40°C suggests fluids from NaCl/$CaCl_2$ of around 1.3 to 0.6 mass ratio, implying some Ca dominant fluids (Oakes et al., 1990). Population C inclusions can be inferred to correlate with D3 extensional re-activation of the main shear zone identified by Bell et al. (2017a,b). Trapping conditions can be unequivocally linked to the temperatures derived from arsenopyrite chemistry by Kaltoft et al., (2000), which for isochores calculated assuming a pure NaCl fluid would indicate trapping pressures from ~100-400MPa. This would suggest minimum depths of ~3-7km, again with super-lithostatic pressures between rupture events, and rapid decompression on rupture accounting for the range in T_h L-V. The data are consistent with initial shear zone and main vein formation near peak metamorphic conditions (Upper Greenschist to Amphibolite facies), and then normal reactivation and quartz-carbonate-sulphide vein formation on the retrograde path during exhumation at lower Greenschist facies conditions.

The population D inclusions are low salinity and inferred to relate to late brittle faulting of the shear zone system (Bell et al., 2017a, b). Comparison of temperatures derived from the Na/K

geothermometer of Can (2002; 200-400°C) with isochores for this population suggest trapping pressures from 100-400MPa, but with a less dramatic pressure cycling than in other populations. The overall process at this point is likely to have been cooling and decompression to lower Greenschist facies or lower during exhumation (indicated by the epidote-zoisite-prehnite-muscovite alteration assemblage; Bell et al., 2017b).

Fluid chemical evolution during mineralisation of the Nalunaq shear zone.

The fluid inclusions analysed in this study preserve an extremely large range in composition, from hypersaline brines (30 to >40 wt % NaCl eq.) to extremely low salinity fluids (<2 wt. % NaCl eq.). The hypersaline brines are strongly distinct from fluids typically related to orogenic gold deposits (meso- or hypo-thermal) where fluids are entirely derived from metamorphic dewatering of hydrous silicates (Groves et al., 1998; Ridley and Diamond, 2000; Garofalo et al., 2014; Goldfarb and Groves 2015). Previous workers have related the high salinity (Kaltoft et al., 2000) of the Nalunaq fluid inclusions to a potential magmatic source (Schlatter and Olsen, 2011; Bell et al., 2017b). High salinity brines can be generated in metamorphic systems if the pre-metamorphic sedimentary system included significant evaporite deposits (Yardley and Graham, 2002). This possibility cannot be ruled out in this context, but there is little evidence of meta-evaporitic layers in the immediate surrounding of Nalunaq (Kaltoft et al., 2000; Schlatter and Olsen, 2011; Bell et al., 2017a,b). A magmatic origin is therefore likely.

The major cation chemistry of the D2-related fluid inclusions is not indicative of a single fluid source. The data are indicative of mixing between an Na-K-Fe-(Sr) dominant and a Ca-dominant brine (Table 2; Fig. 12). There is no correlation between Na/Ca ratio and bulk salinity so the population A and B fluid inclusions do not represent compositional endmembers in this sense, but separate influxes of fluid into the shear zone system driven by the transient pressures drops from fault valve events (Sibson et al., 1988; Sibson, 2004). The controls on the major ion chemistry in the 2 end members must come from

equilibration with source mineral assemblages, equilibration with host rock alteration mineral assemblages, mineral breakdown or precipitation at conditions removed from equilibrium, and variation in the externally controlled variables (P and T) for all these potential chemical conditions (Giggenbach,1988; Yardley, 2005). All fluids show Mg contents that are in excess of the equilibrium concentrations expected for fluids equilibrated with chlorite-muscovite-K-feldspar-albite assemblages (Giggenbach, 1988). Chlorite is of relatively limited distribution as a vein phase in the samples studied, and linked mainly to D4 stage alteration (Bell et al., 2017a), and equilibrium Mg contents in this system are likely to be controlled by the system hornblende-biotite-clinopyroxene in the metabasites, and by clinopyroxene-chlorite and clinopyroxene-zoisite reactions in the later stage (D3-4) calc-silicate alteration. In all these cases the Mg-phase destroying reactions during alteration mean that the Mg contents of the hydrothermal fluids have not equilibrated. At very late stages (D4) clinopyroxene breaks down to zoisite (Bell et al., 2017a), further enriching the fluid in Mg and causing chlorite supersaturation. The precipitation of calcite at the D3 stage may also exert some control on Mg contents in the fluid, but the calcite has not been noted to be particularly Mg-rich.

Equilibration with assemblages containing 2 feldspars produces fluids that become progressively more Na-rich relative to K and Ca with cooling (Giggenbach, 1988; Can 2002) and albite, Ca-plagioclase and K-feldspar are all widespread in host rocks and veins. The Na-rich fluids produce geologically reasonable temperatures when using the Na/K ratio geothermometers, whereas the Ca-rich fluids must have equilibrated with such an assemblage at much higher T (>400°C), or have exceeded the buffer capacity of an equilibrating assemblage through the destruction of potassium phases. Calcium contents of geothermal fluids are strongly dependant on CO_2 fugacity, and linked to calc-silicate breakdown reactions and the formation of calcite. It seems likely that the high salinity Na-rich fluids are derived from granitoid source rocks, a concept which is supported by the generation of biotite within alteration assemblages and the minor K-feldspar present in vein samples (Fig. 4). The Ca-rich fluids are likely to have

their Ca-content controlled by reaction with plagioclase and calcite. Anorthite-albite control on the Ca^{2+}/Na^{+} ratio of the fluids is not strongly sensitive to pH and salinity, and is unlikely to produce Ca-dominant brines (Orville, 1972; Yardley, 2005). There are, however, calcareous metasediments present in the Nanortalik nappe sequence (Petersen, 1993; Kaltoft et al., 2000; Bell et al., 2017a,b) which could have acted as a source of Ca. The two endmember fluids compositions therefore are inferred to be of a granitoid-sourced magmatic fluid, and an equally saline (so therefore probably also magmatically sourced) fluid that had interacted with Ca-rich lithologies in the host nappe sequence. The behaviour of Sr can be explained by the same processes and helps to support these hypotheses. Strontium concentration overall is a simple function of salinity (Fig. 12 D, E), but elevated Sr contents relative to Ca are clearly associated with the Na-rich population noted above, with the lowest Ca/Sr ratio corresponding to the Na-rich end member. The lack of positive correlation between Ca and Sr supports the interpretation that elevated Ca fluids derived from interaction with metasedimentary carbonates rather than from plagioclase destruction. Strontium lost to fluid during plagioclase breakdown is typically re-incorporated into Ca minerals (Zihlmann et al., 2018), and hence high Sr is likely to be a function of the magmatic fluid source. Strontium overall will be controlled by the formation and destruction of calc-silicate minerals and the deposition of carbonate within the vein system. Although Sr partitioning into calcite has been shown to decrease with temperature up to ~100°C (Rimstidt et al., 1998), higher temperature experimental data are lacking. In calcite from the Troodos ophiolite Wiezierl et al., (2018) noted a decrease in Sr in calcite with higher T deposition, and higher fluid Sr concentrations. High Sr concentrations are likely, therefore, to reflect source contributions in the primary fluid, and a lack of buffering of Sr contents by calcite deposition in the shear zone veins system. Intermediate concentrations and ratios are controlled by mixing between end member compositions.

Salinity variations within these populations were driven by loss of water to the carbonic phase during aqueous carbonic phase separation outside of the main shear zone (Bowers and Helgeson, 1983;

Vallance et al., 2009), or variations in the state of evolution of the magmatic source during periods of fluid release to the shear zone system (Cline and Bodnar, 1991). The interaction of both these fluids with the Ca-rich amphibolite assemblage at T in excess of 400°C resulted in the skarn-like clinopyroxene-plagioclase-garnet alteration assemblage (Zhang and Saxena, 1991) associated with the D2 main vein. Seismic pumping of both fluid reservoirs during decompression episodes drove their mixing. The identification of a potential magmatic source is more problematic. Bell et al. (2017a) showed that the main vein and extensional plagioclase-quartz veins formed at 1783+/-9Ma (U-Pb titanite) and aplite dykes and sills have zircon U-Pb dates of 1770+/-22Ma, and so consequently could represent fluid reservoirs for the main vein system.

The post-D2 fluids show cation ratios that do not lie outside the extremes defined for the D2 hypersaline fluids, but reconstructed absolute concentrations show the general trend of dilution with evolution of the vein system. This indicates a shift from a process of mixing between igneous and host meta-igneous and meta-sedimentary equilibrated brines, to a mixing with additional end-members of very low salinity (Fig. 9; Fig. 12). Of these, moderate salinity brines (Population C; 5-10 wt. 5 NaCl eq.) show low Na/Ca ratios and may represent a fluid formed by metamorphic dehydration reactions, released on decompression along the retrograde exhumation path (D3 quartz-carbonate-sulphide veins), and the very low salinity inclusions (Population D) may represent meteoric fluids, entering the system during D4 extensional faulting. Within these fluids, iron shows a strong correlation with salinity and largely follows a dilution trend (Fig. 13a), except for elevated iron concentrations in low salinity secondary inclusions from sample 4 and 5 (D3 fluids). These inclusions also have slightly elevated Fe/Mn ratios, indicative of lower fO_2 and hence higher Fe solubility for a given temperature and salinity (Yardley, 2005).

Gold transport.

The variation in Au concentration with salinity compared to transition metals is shown in Figure 13. The prime control on transition metal concentration through all samples is the salinity and hence the chloride ion concentration and the formation of $[M^{n+}mCl^{-}]^{n-m}$ type complexes (Yardley, 2005). There is some influence from redox state, most notably for Fe, but also for Zn, with enhanced solubility of Fe at lower fO_2 because of the preponderance of Fe^{2+} in solution. The Fe concentration will in part be controlled by the presence of mafic silicates in the source and deposit wall rocks, and partly by the sulphide assemblage. Zinc and lead correlate strongly and their concentration will be controlled by equilibrium with sphalerite and galena in source rocks and within the vein. The dominant sulphide assemblage within the D2 quartz of the main vein and quartz plagioclase vein samples studied here includes chalcopyrite and arsenopyrite, whilst Bell et al., (2017a) also identified pyrrhotite within the wall rock assemblages, and sphalerite in the quartz-plagioclase veins and calc-silicate alteration zones. Within the Au-bearing quartz-calcite veins we have observed chalcopyrite, pyrite, arsenopyrite and pyrrhotite. This matches the assemblage noted by Bell et al. (2017a), with the addition of löllingite in the biotite-arsenopyrite alteration selvage. The assemblage pyrite-arsenopyrite-pyrrhotite at ~350°C and arsenopyrite-löllingite-pyrrhotite at ~500°C fix the log fS_2 at ~-8 to -10 (Kretschmar and Scott, 1976; Sharp et al., 1985; Sui et al., 2017). Magnetite is not present in the wall rock assemblage, but the pyrite-pyrrhotite assemblages suggests log fO_2 may have been around or below -27 to -34 at 350°C, at a range of pH (Hayashi and Ohmoto, 1991; Gibert et al., 1998). Slightly lower oxygen fugacities inferred for D3 stage secondary inclusions in samples 4 and 5 may relate to interaction with the more reduced, ilmenite-bearing (Bell et al., 2017) metabasic host rock assemblage.

The fluid flow conditions estimated here exceed the P-T conditions of most experimental studies, and the measured Au contents of fluid inclusions are orders of magnitude higher than those determined in those studies. Louks and Mavrogenes (1999), however, studied gold solubility in brines using synthetic fluid inclusions under conditions which are a close match to those determined here (550-725°C; 100-

400MPa; $fO2$ buffered by pyrite-magnetite-pyrrhotite equilibrium; pH buffered by K-feldspar-muscovite-quartz equilibrium; ~6 wt. % NaCl eq.). Under these conditions Au concentrations of 1180+/-390ppm were measured at 625°C and 400MPa, declining to 61+/-15ppm at 110MPa (without effects from phase separation). The P-T-pH-fO_2-fS_2 conditions are comparable to at least some of the conditions at Nalunaq, and the D3 stage fluids have comparable salinities, although the D2 fluids are significantly more saline. Experiments by Frank et al. (2002) show that Au solubility is independent of Cl concentration below $1.1x10^4$ppm HCl (~18 wt. % NaCl eq.). Guo et al. (2018) measured Au solubilities of up to 1000-3000ppm in saline fluids (up to 50 wt. % NaCl eq.) at 600°C and 100MPa with $fO2$ buffered by the hematite-magnetite assemblage, and inferred Au transport dominantly as $AuCl^0$ and $AuCl_2^-$ species. Gammons and Williams-Jones (1995) and Williams-Jones et al. (2009) suggested that a shift to Cl-complexation should occur at ~360°C at conditions between the hematite-magnetite and pyrite-magnetite-pyrrhotite buffer, with pH buffered by k-feldspar-muscovite-quartz. However, their analysis did not include the high P data of Louks and Mavrogenes (1999). In addition, Gibert et al. (1998) suggested that between 250 and 450°C the shift from Cl- dominated gold species to HS^- dominated at 50MPa occurred at ~pH 5, and hence that Cl-complexes would only dominate at acid pH. It is therefore unlikely that Cl-complexation had a major role in Au transport in the low and intermediate salinity D3 and D4 fluids because of the low overall chlorinity, the low fO_2, and the near neutral pH (buffered by K-feldpsar-muscovite-quartz). For the hypersaline D2-3 fluid the low $fO2$ and near neutral pH still pertain, and again Cl-complexation of gold is unlikely. Given these constraints the data and analysis of Louks and Mavrogenes (1999) provide the best model for Au transport and deposition at Nalunaq.

The first fluids recorded in the main vein system at Nalunaq are brines of ~30 wt. % NaCl eq. in samples 3 and 4, with inferred trapping conditions of ~300-400C and 200-900MPa. The upper limit of Au measured in these fluids is ~250-300ppm (Fig. 13), which is exceeds the upper limit of solubility at that T from Louks and Mavrogenes (1999, 10-100ppm) but is consistent with solubilities at higher T (up to

1180ppm at 625°C). The pressure conditions inferred here also exceed the upper pressure limit of experimental data. The elevated Au concentrations are therefore likely related to transport as the high pressure complex $AuHS(H_2S)_3^0$. Decompression of such a fluid would cause dramatic reductions in Au solubility to <1ppm, accounting for Au deposition and the reduction of Au concentration in most fluids to below detection limits (Fig. 16). These fluids are likely to be magmatic in origin, as is the contained Au, linked to the aplite dykes as the earliest magmatic stage in the area.

The latest D2/early D3 fluid recorded in the main vein, and the cross-cutting quartz feldspar veins show more extreme salinities (30-45 wt. % NaCl eq.), potentially derived initially from magmatic sources, but with salinity enhanced by wall-rock interaction and aqueous-carbonic phase separation (Kaltoft et al., 2000). The Au content of these fluids is lower than in the main D2 fluids (10-200ppm), and probably influenced by reduction in fS_2 by sulphidation of wall rocks (Bell et al., 2017a,b) and fluid immiscibility (Kaltoft et al., 2000; Duan et al., 1996) and, again, by cyclic pressure drops during rupture of the shear system. The measured Au contents are consistent with the data of Louks and Mavrogenes (1999) for T in excess of 450°C (Fig. 16). The later D3 fluids (sample 5, 7) are inferred to result from mixing with lower salinity brines, and ultimately with meteoric water (Fig. 9), and correspond to the Au-richest portions of the vein system. Gold concentrations measured at this stage range from ~100-250ppm, at inclusion trapping conditions of 300-400C and ~500-50Mpa. This stage is the most sulphide-rich within the vein system, and Au deposition is inferred to have occurred via reduction in fS_2 by sulphide (arsenopyrite) deposition, coupled with decompression and cooling (Fig. 16). The D4 fluids are inferred to represent meteoric fluid ingress into the shear zone system during later stage normal faulting. They have the lowest measured Au concentrations in this study, with most inclusions below detection limits, and are likely to be mainly responsible for Au redistribution during oxidation of arsenopyrite (see below).

Post-formation modification.

Although the majority of Au at Nalunaq is present as independent grains of coarse gold, gold also occurs in association with the sulphide mineral assemblage, and in particular with arsenopyrite (Fig. 4h). Our SEM observations (Fig. 5) show that particulate Au is hosted within hematite/goethite rims developed during the oxidation of arsenopyrite. Bell et al. (2017) inferred Fe-oxide assemblages within the Nalunaq vein system to have formed during the D4 brittle normal faulting event, which the fluid inclusion data presented here suggest was accompanied by the ingress of very low salinity meteoric derived fluids. X-ray photoelectron spectroscopic observations of the oxidation products indicate the presence of hematite/goethite, Fe(II) oxide and Fe (III) sulphate (Fig. 14a), consistent with typical low T Fe oxidation products of arsenopyrite described by Corkhill and Vaughn (2009).

The Au4f7/2 peak at 84.0ev is clearly resolved in the XPS spectra of the arsenopyrite oxidation products (Fig. 14G) indicating the presence of metallic Au. The Au4f5/2 peak (88.1eV) can be resolved as a shoulder on the margin of the much large Fe 3s peak at 91eV. These binding energies are significant as the Au 4f7/2 peak at 83.95eV is characteristic of Au^{+} as well as Au^{0} (Kitagawa et al., 1991). Reiche et al. (2005) argued that the solubility of Au within arsenian pyrite as Au^{+} is limited by a maximum molar ratio of 0.02, and that above this limit gold is present as nanoparticulate metallic Au. The data presented here are therefore consistent with the known solubility of Au in sulphides, and with the release of Au^{+} from the arsenopyrite lattice during oxidation and its reduction to Au^{0}. Although this is a relatively minor form of Au within the deposit, oxidation of arsenopyrite during either epithermal circulation during normal faulting, or during subsequent weathering of the deposit, forms an additional route for gold grain formation and for enhancing the grade heterogeneity of the deposit (Dominy and Petersen, 2005).

Implications.

The structural setting of the Nalunaq gold deposit is clearly consistent with general models for orogenic gold deposits. However, the fluid characteristics associated particularly with early stages of gold-bearing vein formation are not the same as typical mesothermal orogenic gold systems. The fluid inclusion microthermometric characteristics and chemistry strongly support mixing of fluids of several different sources or water-rock interaction histories, including magmatic fluids, magmatic fluids modified by an extensive history of wall rock alteration and aqueous carbonic immiscibility, fluids derived from metamorphic dehydration reactions and meteoric water. Goldfarb and Groves (2015) suggested that mixing of different fluid sources would not occur in orogenic gold deposits as systems were over-pressured, and hence fluids would be expelled from vein systems rather than drawn in. The arguments against mixed fluid sources disregard the evidence from some studies (e.g. Neumayr et al 2007), the fact that tectonic deformation, metamorphism and magmatism are intrinsically interlinked in most mountain belts, and hence a range of fluid reservoirs are present in any given environment, and the presence of high temperature alteration assemblages in some deposits that are directly comparable to skarns (e.g. Kolb et al., 2015). The argument for over-pressure preventing fluid ingress and mixing also does not take into account the large pressure drops possible on rupture, and hence the drawing of fluid into dilation zones during transient sub-lithostatic pressure periods (seismic pumping - Sibson et al., 1988; Walshe et al., 2003).

The early stage, skarn-like alteration forming fluids at Nalunaq have close parallels in hypozonal lode gold systems (Groves et al., 1998). Hypozonal systems have been described as showing As-dominated sulphide assemblages (Groves et al., 1998), with alteration assemblages typical of high P (>3kbar) and T (typically greater than 500°C) including calc-silicate (garnet-pyroxene-amphibole) and potassic (Biotite-K-feldspar) assemblages (McCuaig et al., 1993; Kolb et al., 2015). We propose that Nalunaq forms an example of the hypozonal class, transitional to mesothermal conditions as the system evolved, with repeated injections of hydrothermal fluids from deep, overpressure reservoirs, the surrounding

metamorphic pile, and, during the exhumation of the system on normal faults, meteoric fluids (c.f. Menzies et al., 2014). Kolb et al. (2015) suggested a mineral systems view of hypozonal lode gold deposits, whereby they formed in syn- to post-peak metamorphic shear zones of high metamorphic grade terranes in the centre or foreland of Precambrian accretionary and collisional orogens, particularly post-active subduction during active uplift. The setting of Nalunaq, in the fore-arc to the Julianehåb igneous complex (Chadwick and Garde, 1996; Garde et al., 2002) in a meta-sedimentary and meta-igneous rock sequence inferred to have been deposited during arc exhumation, is entirely consistent with this model. The multiple fluid sources, developing from peak metamorphic conditions through deformation and exhumation of the Nanortalik nappe, are likely to be characteristic of such systems.

Conclusions.

The Nalunaq deposit, Greenland, is a hypozonal, shear zone-hosted Au deposit. The shear zone system was initially infiltrated by hypersaline brines (~30 wt. % NaCl eq.) inferred to be sourced from local granitoids at 300-475°C, with flow driven by decompression during shear zone movement drawing fluid into dilational zones. The fluid evolved to higher salinity, and in major cation contents, by interaction with metabasic and potentially carbonate wall rocks, aqueous-carbonic fluid immiscibility and mixing between repeated batches of fluid infiltration. The fluid chemistry was subsequently modified by dilution during extensional reactivation at 300-400°C, resulting in formation of carbonate-quartz sulphide veins which host the highest gold grades. The final phase of fluid flow recorded by fluid inclusions is the ingress of low salinity fluids, inferred to be of meteoric origin during post-orogenic extension which mixed with residual higher salinity fluids. Gold contents have been measured in a limited number of fluid inclusions preserved from each stage of the systems evolution. High concentrations are consistent with Au transport at high P and T (>400Mpa, 300-475°C) as $AuHS(H_2S)_3^0$ complexes, which were destabilised on decompression resulting in gold precipitation during D2 and D3 times. Gold also occurs associated with sulphide minerals

(arsenopyrite) and was released as a result of sulphide oxidation during D4 extensional faulting, or subsequent exhumation and wreathing resulting in further nugget formation. Overall the system represents a key example of a hypozonal system with evidence of multiple fluid sources and mixing driven by fault valve action and seismic pumping.

Acknowledgements

The microthermometric data in this paper were originally commissioned by Angle Mining Plc. and the authors would like to thank Angel Mining Plc. for permission to publish these data. Laser Ablation-ICPMS analyses were carried out at the NERC JIF sponsored facility at the University of Leeds, U.K. (NER/H/S/2000/853). X-ray photoelectron spectroscopy was carried out at the Surface Analysis Laboratory which is jointly funded by NERC (RCUK) and the University of Brighton.

Author Contributions

MS: conceptualisation (lead), investigation (lead), data curation (lead), methodology (equal), formal analysis (lead), writing – original draft (lead), writing – review and editing (lead); **DB:** methodology (equal), formal analysis (equal), writing – original draft (supporting), writing – review and editing (supporting); **SR:** methodology (equal), formal analysis (equal), writing – original draft (supporting), writing – review and editing (supporting); **FB:** conceptualisation (supporting), investigation (supporting) methodology (equal), resources (lead).

Fluid inclusion data generated during this study are included in this published article (and its supplementary information files). Unprocessed XPS data in Thermo Avantage format are available from the authors on reasonable request.

References

Allan M.M.; Yardley, B.W.D.; Forbes, L.J., Shmulovich, K. I., Banks, D.A. and Shepherd, T.J. (2005).Validation of LA-ICP-MS fluid inclusion analysis with synthetic fluid inclusions. American Mineralogist, 90, 1767-1775

Archer, D.G., (1992) Thermodynamic properties of the NaCl +H2O system: II. Thermodynamic properties of NaCl(aq), NaCl.2H2O(cr), and phase equilibria. Journal of Physical Chemistry Reference Data 28, 1 – 17.

Bakker R.J. (2003) Package FLUIDS 1. Computer programs for analysis of fluid inclusion data and for modelling bulk fluid properties. Chemical Geology 194, 3-23.

Banks, D., Bozkaya, G., Bozkaya, O. (2018) Direct Observation and Measurement of Au and Ag in Epithermal Mineralizing Fluids. *Ore Geology Reviews*, doi:https://doi.org/10.1016/j.oregeorev.2019.102955

Becker S.P.; Fall A.; Bodnar R.J. (2008) Synthetic fluid inclusions. XVII. PVTX properties of high salinity H2O-NaCl solutions (> 30 wt % NaCl): Application to fluid inclusions that homogenize by halite disappearance from porphyry copper and other hydrothermal ore deposits. Economic Geology 103, 539-554.

Bell, R.M., Kolb, J., and Waight, T.E. (2017a) Assessment of lithological, geochemical and structural controls on gold distribution in the Nalunaq gold deposit, South Greenland using three-dimensional implicit modelling. In Gessner, K., Blenkinsop, T., and Sorjonen-Ward P. (eds) Characterization of Ore-Forming Systems from Geological, Geochemical and Geophysical Studies. Geological Society, London, Special Publications, 453, https://doi.org/10.1144/SP453.2

Bell, R.M., Kolb, J., Waight, T.E., Bagas, L., and Thomsen T.B. (2017b) A Palaeoproterozoic multi-stage hydrothermal alteration system at Nalunaq gold deposit, South Greenland. Mineralium Deposita 52, 383–404.

Bodnar, R.J., 1993. Revised equation and table for determining the freezing point depression of H2O–NaCl solutions. *Geochimica et Cosmochimica Acta* 57, 683–684.

Boue-Bigne F.; Masters B.J.; Crighton J.S. and Sharp B. L. (1999) A calibration strategy for LA-ICP-MS analysis employing aqueous standards having modified absorption coefficients. Journal of Analytical Atomic Spectroscopy 14, 1665-1672.

Bowers T.S. and Helgeson H.C. (1983) Calculation of thermodynamic and geochemical consequences of non-ideal mixing in the system H_2O-CO_2-NaCl on phase relations in geologic systems: Equation of state for H_2O-CO_2-NaCl fluids at high pressures and temperatures. Geochimica et Cosmochimica Acta, 47, 1247-1275

Can, I. (2002) A new improved Na/K geothermometer by artificial neural networks. Geothermics 31, 751–760.

Chadwick B, Garde AA (1996) Palaeoproterozoic oblique plate convergence in South Greenland; a reappraisal of the Ketilidian Orogen. In: Brewer TS (ed) Precambrian crustal evolution in the North Atlantic region. Geological Society Special Publications 112: 179-196

Cline, J. and Bodnar, R. (1991) Can economic porphyry mineralisation be generated by a typical calc-alkaline melt? Journal of Geophysical Research, 96, 8113-8126.

Corkhill, C.L. and Vaughn, D.J. (2009). Arsenopyrite oxidation – A review. Applied Geochemistry 24, 2342–2361

Micklethwaite, S. and Cox, S. (2006) Progressive fault triggering and fluid flow in aftershock domains: examples from mineralized Archaean fault systems. Earth and Planetary Science Letters, 250, 318-330.

Dominy S.C. and Petersen, J.S. (2005) Sampling Coarse Gold-Bearing Mineralisation — Developing Effective Protocols and a Case Study From the Nalunaq Deposit, Southern Greenland. Sampling and Blending Conference proceedings, Queensland. Pp. 151-165.

Duan Z., Moller N., Weare J.H. (1996) Prediction of the solubility of H_2S in NaC1 aqueous solution: an equation of state approach. Chemical Geology 130, 15-20

Frank, M.R., Candela, P.A., Piccoli, P., Glascock, M.D. (2002) Gold solubility, speciation, and partitioning as a function of HCl in the brine-silicate melt-metallic gold system at 800°C and 100 MPa. Geochimica et Cosmochimica Acta, Vol. 66, 3719–3732.

Gammons, C.H. and Williams-Jones, A.E. (1995) The solubility of Au-Ag alloy + AgCl in HCl/NaCl solutions at 300 °C; new data on the stability of Au(I) chloride complexes in hydrothermal fluids. Geochimica et Cosmochimica Acta 59 (1995), pp. 3453-3468

Gammons, C.H., Yu, Y., and Williams-Jones, A.E. (1997) The disproportionation of gold(I) chloride complexes at 25 to 200°C. Geochimica et Cosmochimica Acta, 61, 1971-1983.

Garde, A.A., Hamilton, M.A., Chadwick, B., Grocott,J. & McCaffrey, K.J.W. 2002a. The Ketilidian orogen of South Greenland: geochronology, tectonics, magmatism, and fore-arc accretion during Paleoproterozoic oblique convergence. Canadian Journal of Earth Science, 39, 765–793.

Garofalo, P.S., Fricker, M.B., Günther, D., Bersani, D., Lottici, P.P. (2014) Physical-chemical properties and metal budget of Au-transporting hydrothermal fluids in orogenic deposits. In Garofalo, P. S. and Ridley, J. R. (eds) Gold-Transporting Hydrothermal Fluids in the Earth's Crust. Geological Society, London, Special Publications, 402, http://dx.doi.org/10.1144/SP402.8.

Gibert, F., Pascal, M.-L., and Pichavant, M. (1998) Gold solubility and speciation in hydrothermal solutions: Experimental study of the stability of hydrosulphide complex of gold (AuHS°) at 350 to 450°C and 500 bars. Geochimica et Cosmochimica Acta, 62, 2931–2947

Giggenbach, W.F. (1988) Geothermal solute equilibria. Derivation of Na-K-Mg-Ca geoindicators. Geochimica et Cosmochimica Acta, 52, 2749-2765.

Goddard, R. (2009) Nalunaq gold mine: A synthesis of the developments in understanding of the ore genesis and geological controls on grade from early exploration through to recent extraction. Report to Angel Mining. 29pp.

Goldfarb, R.J. and Groves, D.I. (2015) Orogenic gold: Common or evolving fluid and metal sources through time. Lithos 233, 2–26.

Groves, D.I., Goldfarb, R.J., Gebre-Mariam, M., Hagemann, S., and Robert, F. (1998) Orogenic gold deposits: A proposed classification in the context of their crustal distribution and relationship to other gold deposit types. Ore Geology Reviews 13, 7–27

Groves, D.I., Goldfarb, R.J., Robert, F., and Hart, C.J.R. (2003) Gold Deposits in Metamorphic Belts: Overview of Current Understanding, Outstanding Problems, Future Research, and Exploration Significance. Economic Geology 98, 1–29

Günther D., Frischknecht R., Muschenborn H.J., and Heinrich C.A. (1997) Direct liquid ablation: a new calibration strategy for laser ablation ICP-MS microanalysis of solids and liquids. Fresenius Journal of Analytical Chemistry 359, 390-393.Guo et al., 2018

Hayashi, K.-I., and Ohmoto, H. (1991) Solubility of gold in NaCl- and H2S-bearing aqueous solutions at 250-350°C. Geochimica et Cosmochimica 55, 21, I I-2126.

Heinrich C.A., Günther D., Audétat A., Ulrich T., and Frischknecht R. (1999) Metal fractionation between magmatic brine and vapor, determined by microanalysis of fluid inclusions: Geology, 27, 755–758.

Huntley D.R., Overbury S.H., Zehner D.M., Budai J.D., Brower W.E., (1986) Surface characterization of amorphous and crystallized $Fe_{80}B_{20}$. Applied Surface Science 27, 180-198.

Kaltoft, K., Schlatter, D.M., and Kludt, L. (2000) Geology and genesis of Nalunaq Palaeoproterozoic shear zone hosted gold deposit, south Greenland. Transactions of the Institute of Mining and Metallurgy B:Applied Earth Sciences, 109, 23-33.

Kishida, A. and Kerrick, R. (1987) Hydrothermal alteration zoning and gold concentration at the Kerr Addison Archean lode gold deposit, Kirkland Lake, Ontario. Economic Geology, 82, 649-690.

Kitagawa H., Kojima N., Nakajima T. J. (1991) Studies of mixed-valence states in three-dimensional halogen-bridged gold compounds, $Cs_2Au^{I}Au^{III}X_6$, (X = Cl, Br or I). Part 2. X-Ray photoelectron spectroscopic study. Journal of the Chemical Society, Dalton Transactions 11, 3121-3125.

Kolb, J., Rogers, A., Meyer, F.M., Vennemann, T.W. (2004) Development of fluid conduits in the auriferous shear zones of the Hutti Gold Mine, India: evidence for spatially and temporally heterogeneous fluid flow. Tectonophysics 378, 65–84.

Kolb, J., Dziggel, A., and Bragas, L. (2015) Hypozonal lode gold deposits: A genetic concept based on a review of the New Consort, Renco, Hutti, Hira Buddini, Navachab, Nevoria and the Granites deposits. Precambrian Research 262, 20–44.

Kretschmar, U., Scott, S.D. (1976) Phase relations involving arsenopyrite in the system Fe-As-S and their application. Canadian Mineralogist 14, 364–386.

Kwak T.A.P., Brown W.M., Abeysinghe P.B., Tan T.H. (1986) Fe solubilities in very saline hydrothermal fluids - their relation to zoning in some ore-deposits. Economic Geology 81, 447-465.

Lecumberri-Sanchez, P., Steele-MacInnis, M., Bodnar, R.J. (2012) A numerical model to estimate trapping conditions of fluid inclusions that homogenize by halite disappearance. Geochimica et Cosmochimica Acta, 92, 14-22.

Louks, R.R. and Mavrogenes J.A. (1999) Gold Solubility in Supercritical Hydrothermal Brines Measured in Synthetic Fluid Inclusions. Science, 284, 2159-2163.

Marcus P., Grimal J.M. (1992) The anodic dissolution and passivation of Ni-Cr-Fe alloys studies by ESCA. Corrosion Science 33, 805.

McCuaig, T.C. and Kerrich, R. (1998) P-T-t-deformation-fluid characteristics of lode gold deposits: evidence from alteration systematics. Ore Geology Reviews 12, 381-453.

Meinert, L.D. (1993) Skarns and skarn deposits. Geoscience Canada, 19, 145-162.

Menzies, C.D., Teagle, D.A.H., Craw, D., Cox, S.C., Boyce, A.J., Barrie, C.D. Roberts, S. (2014) Incursion of meteoric waters into the ductile regime in an active orogen. Earth and Planetary Science Letters 399, 1–13

Mills P., and Sullivan J.L. (1983) A study of the core level electrons in iron and its three oxides by means of X-ray photoelectron spectroscopy. Journal of Physics D. 16, 723

Nesbitt, H.W. and Reinke, M. (1999) Properties of As and S at NiAs, NiS, and $Fe_{1-x}S$ surfaces, and reactivity of niccolite in air and water. American Mineralogist, 84, 639-649.

Neumayr, P., Walshe, J., Hagemann, S., Petersen, K., Roache, A., Frikken, P., Horn, L., and Halley, S. (2007) Oxidized and reduced mineral assemblages in greenstone belt rocks of the St. Ives gold camp, Western Australia: vectors to high-grade ore bodies in Archaean gold deposits. Mineralium Deposita 43, 363–371.

Oakes C.S., Bodnar R.J. and Simonson J.M. (1990) The system NaCl-$CaCl_2$-H_2O .1. The ice liquidus at 1 atm total pressure. Geochimica et Cosmochimica Acta, 54, 603-610.

Orville, P.M., 1972, Plagioclase ion exchange equilibria with aqueous chloride solutions: Results at 700°C and 2000 bars in the presence of quartz: American Journal of Science, 272, 234–272.

Petersen, J.S. 1993. Results of Geological Investigation on Gold Mineralization in the Nalunaq Area, Nanortalik Peninsula, SW Greenland. GEUS Report 21357. NunaOil, Nuuk, Greenland.

Petersen JS, Olsen HK (1995) Gold exploration in Ippatit area – Søndre Sermilik - Amitsoq island, South Greenland. Internal report, Nunaoil A/S, 25 pp, 5 app, 6 plates. GEUS report number: 21424

Phillips, G.N. and Powell, R. (2015) A practical classification of gold deposits, with a theoretical basis. Ore Geology Reviews 65 (2015) 568–573

Phillips, G.N., Powell, R., 1993. Link between gold provinces. Economic Geology 88, 1084–1098.

Phillips, G.N., Powell, R. (2010) Formation of gold deposits: a metamorphic devolatilization model. Journal of Metamorphic Geol. 28, 689–718.

Rauchenstein-Martinek K, Wagner T, Wälle M, Heinrich CA (2014) Gold concentrations in metamorphic fluids: a LA-ICPMS fluid inclusion study from the Alpine orogenic belt. Chemical Geology, 385, 70– 83.

Reiche, M., Kesler, S.E., Utsunomiya, S., Palenik, C.S., Chryssoulis, S.L., and Ewing, R. (2005) Solubility of gold in arsenian pyrite. Geochimica et Cosmochimica Acta, 69, 2781–2796.

Ridley, J., Mikucki, E.J., and Groves, D.I. (1996) Archean lode-gold deposits" fluid flow and chemical evolution in vertically extensive hydrothermal systems. Ore Geology Reviews 10, 279-293

Ridley J.R. and Diamond L.W. (2000) Fluid chemistry of lode-gold deposits and implications for genetic models. In: Hagemann S.G., Brown P. (Eds.), Gold in 2000. Reviews in Economic Geology. Society of Economic Geologists, Inc., Vol. 13, pp. 141-162.

Rimstidt, J.D., Balog, A., and Webb, J. (1998) Distribution of trace elements between carbonate minerals and aqueous solutions. Geochimica et Cosmochimica Acta, 62, 1851–1863

Robb, L. (2005) Introduction to ore forming processes. Blackwell Science Ltd, Oxford. 373pp.

Schlatter, D.M. and Olsen, S.D. (2011) The Nalunaq gold mine: a reference sample collection and compilation and interpretation of geochemical data. GEUS report 2011/31, 80pp.

Seah M.P., Smith G.C., Anthony M.T. (1990) AES: Energy calibration of electron spectrometers. I—an absolute, traceable energy calibration and the provision of atomic reference line energies. Surface and Interface Analysis 15, 293-308.

Seward, T.M., 1973. Thio complexes of gold and transport of gold in hydrothermal ore solutions. Geochimica et Cosmochimica Acta 37, 379–399.

Sharp, Z.D., Essene, E.J., Kelly, W.C., 1985. A re-examination of the arsenopyrite geothermometer; pressure considerations and applications to natural assemblages. Canadian Mineralogist 23, 517–534.

Sibson, R.H, Robert, F., and Poulsen, K.H. (1988) High angle reverse faults, fluid pressure cycling and mesothermal gold-quartz deposits. Geology 16, 551-555.

Sibson, R.H. (2004) Controls on maximum fluid overpressure defining conditions for mesozonal mineralisation. Journal of Structural Geology 26, 1127–1136

Sillitoe, R. H. (1991) Intrusion-related gold deposits. *in* Gold Metallogeny and Exploration (Foster, R. P., ed.), 165–209. Blackie, Glasgow & London.

Sillitoe, R.H., 2008. Major gold deposits and belts of the North and South American Cordillera-distribution, tectonomagmatic setting, and metallogenic considerations. Economic Geology 104, 663-687.

Siriwardene R. V., Cook J. M. (1985) Interactions of SO_2 with sodium deposited on silica. Journal of Colloid and Interface Science 108, 414-422.

Simon A.C., Frank M.R., Pettke T. (2005) Gold partitioning in melt-vapor-brine systems. Geochimica et Cosmochimica Acta, 69, 3321-3335

Smith, M.P., Gleeson, S.A., Yardley, B.W.D. (2019) Hydrothermal fluid evolution and metal transport in the Kiruna District, Sweden: Contrasting metal behaviour in aqueous and aqueous–carbonic brines. Geochimica et Cosmochimica Acta 102, 89–112.

Spooner, E.T.C., Bray, C.J., Wood, P.C., Burrows, D.R., Callan, N.J., 1987. Au-quartz vein and Cu-Au-Ag-Mo-anhydrite mineralization, Hollinger-McIntyre Mines, Timmins, Ontario: ^{13}C values (McIntyre) fluid inclusion gas chemistry, pressure (depth) estimation, and H_2O-CO_2 phase separation as a precipitation and dilation mechanism. Ontario Geological Survey Miscellaneous Paper 136, 35-56.

Stec W.J., Morgan W.E., Albridge R.G., Van Wazer J.R. (1972) Measured binding energy shifts of "3p" and "3d" electrons in arsenic compounds. Inorganic Chemistry 11, 219-225.

Sterner S. M., Hall D. L. and Bodnar R. J. (1988) Synthetic fluid inclusions. V. Solubility relations in the system NaCl–KCl–H2O under vapour-saturated conditions. Geochimica et Cosmochimica Acta 52, 989–1005.

Sui, J.X., Li, J.W., Wen, G., and Jin, X.Y. (2017) The Dewulu reduced Au-Cu skarn deposit in the Xiahe-Hezuo district, West Qinling orogen, China: Implications for an intrusion-related gold system. Ore Geology Reviews 80, 1230-1244.

Thompson, J.F.H., Sillitoe, R.H., Baker, T., Lang, J.R., and Mortensen, J.K. (1999) Intrusion-related gold deposits associated with tungsten-tin provinces. Mineralium Deposita, 34, 323-334.

Valance, J., Fontbote, L., Chiardia, M., Markowski, A., Schmidt, S., Venneman, T. (2009) Magmatic-dominated fluid evolution in the Jurassic Nambija gold skarn deposits (southeastern Ecuador). Mineralium Deposita, 44, 389–413.

Williams-Jones, A.E., Bowell, R.J., and Migdisov, A. (2009) Gold in solution. Elements, 5, 281-287.

www.xpsfitting.com, 2020. X-ray Photoelectron Spectroscopy (XPS) Reference Pages. Accessed 24/8/2020

Yardley B.W.D. (2005) Metal Concentrations in Crustal Fluids and Their Relationship to Ore Formation. Economic Geology 100, 613-632.

Yardley, B.W.D. and Graham, J.T. (2002) The origin of salinity in metamorphic fluids. Geofluids 2, 249-256.

Yu X.-R., Liu F., Wang Z.-Y., and Chen Y. (1990) Auger parameters for sulfur-containing compounds using a mixed aluminum-silver excitation source. Journal of Electron Spectroscopy and Related Phenomena 50, 159-166.

Zhang Y.G. and Frantz J.D. (1987) Determination of the homogenization temperatures and densities of supercritical fluids in the system NaCl-KCl-CaCl2-H2O using synthetic fluid inclusions. Chemical Geology 64, 335-350.

Zhang, Z. & Saxena, S. K. (1991). Thermodynamic properties of andradite and application to skarn with co-existing andradite and hedenbergite. Contributions to Mineralogy and Petrology 107, 255–263.

Zihlmann, B., Muller, S., Coggon, R.M., Koepke, J., Garbe-Schonberg, D., Teagle D.H. (2018) Hydrothermal fault zones in the lower oceanic crust: An example from Wadi Gideah, Samail ophiolite, Oman. Lithos 323, 103–124.

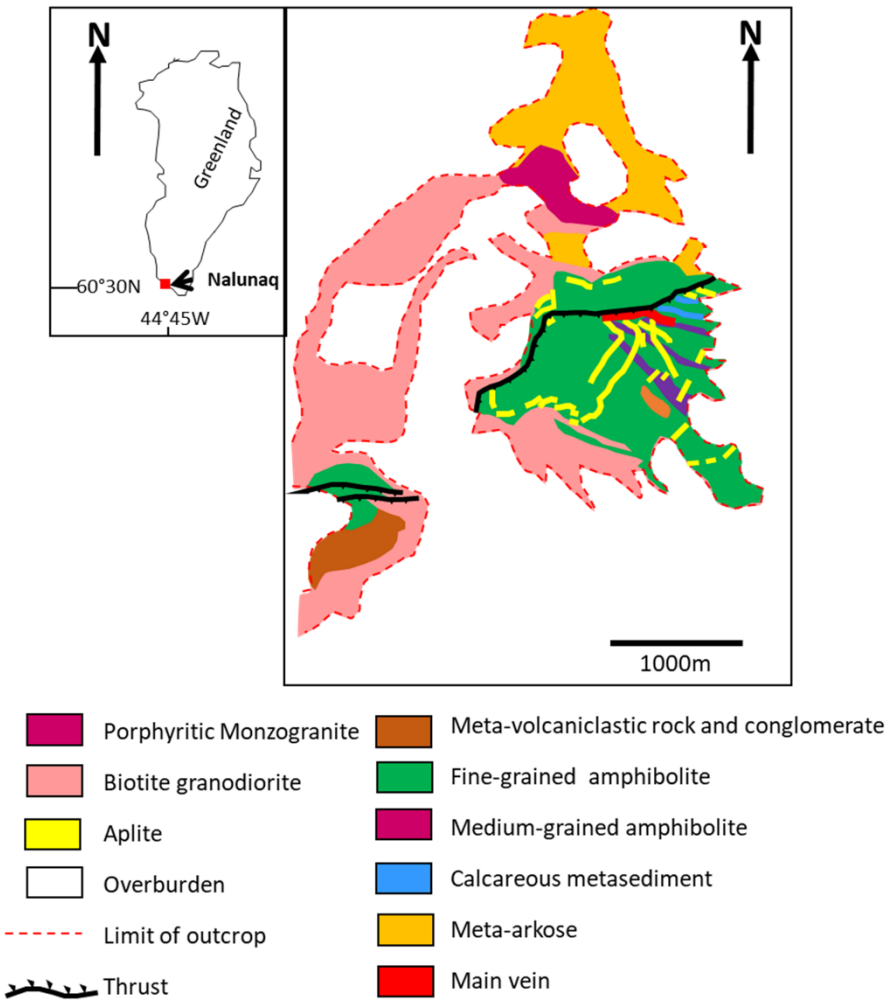

Figure 1: Geological map of Nalunaq Mountain (simplified from Bell et al., 2017a).

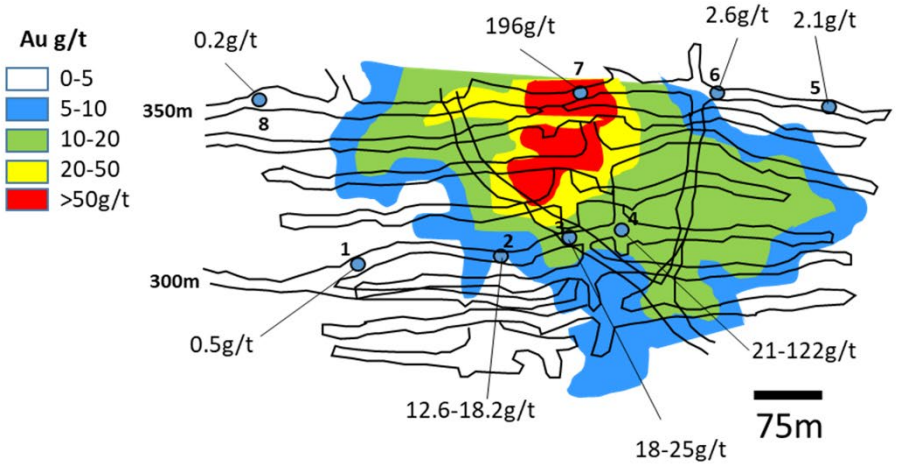

Figure 2: Mine level map, projected vertically, downwards showing sample locations within the 300 and 350m levels of the Nalunaq Target Zone. Grade distribution contours simplified from Bell et al., 2017a.

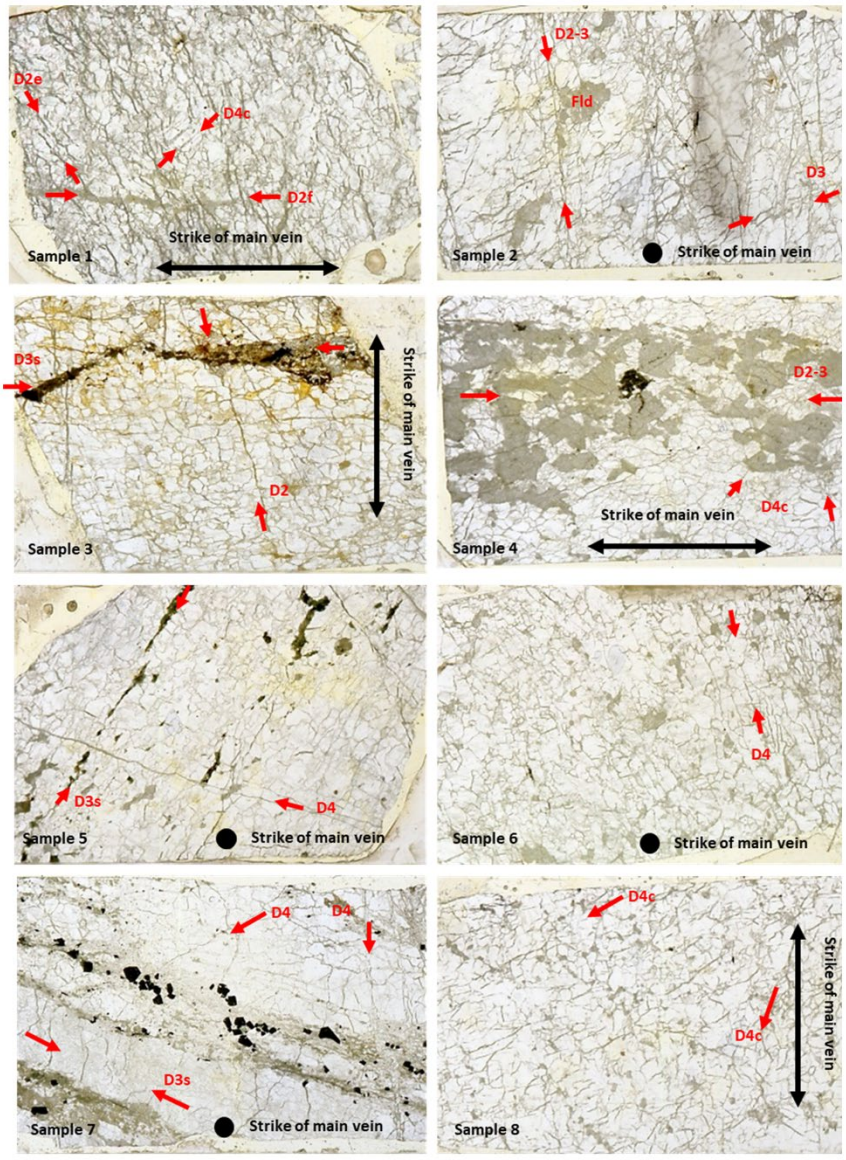

Figure 3: Individual scans of fluid inclusion wafers. Strike of main vein indicated in each case. Deformation stages assigned on the basis of mineralogy, cross cutting relationships and correlation with Bell et al. (2017a, b). **Sample 1** – D2F: Feldspar lined factures, strike subparallel but 30-40° dip angle to main vein. D2e: Healed fractures, near perpendicular to main vein. D4c: Brittle conjugate fracture set. **Sample 2** – D2-3: Main vein parallel fractures associated with quartz sub-grain development, calcite and pyrite. D3: Secondary fractures, possibly conjugate to D2-3. **Sample 3** – D2: Feldspar lined D2 fractures off set by D3s vein. D3s: Main vein strike parallel quartz-sulphide-calcite-chlorite vein, with parallel secondary trails. **Sample 4** – D2-3: Feldspar-quartz vein in conjugate set, strike sub-parallel to main vein. D4c: Brittle conjugate fracture set. **Sample 5** – D3s: Quartz filled fracture with actinolite, magnetite, pyrite, and minor chalcopyrite and pyrrhotite. Strike perpendicular to main vein. D4 – Late stage feldspar lined fracture cross0cutting D3s. **Sample 6** – D4: Main vein strike parallel, cross cutting inclusion trails with conjugate fractures. **Sample 7** – D3s: High angle, cross cutting quartz-calcite-pyrite-pyrrhotite-chalcopyrite vein. D4: Brittle conjugate fracture set, cross cutting D3s. **Sample 8** - D4c: Brittle conjugate fracture set crossing main vein quartz.

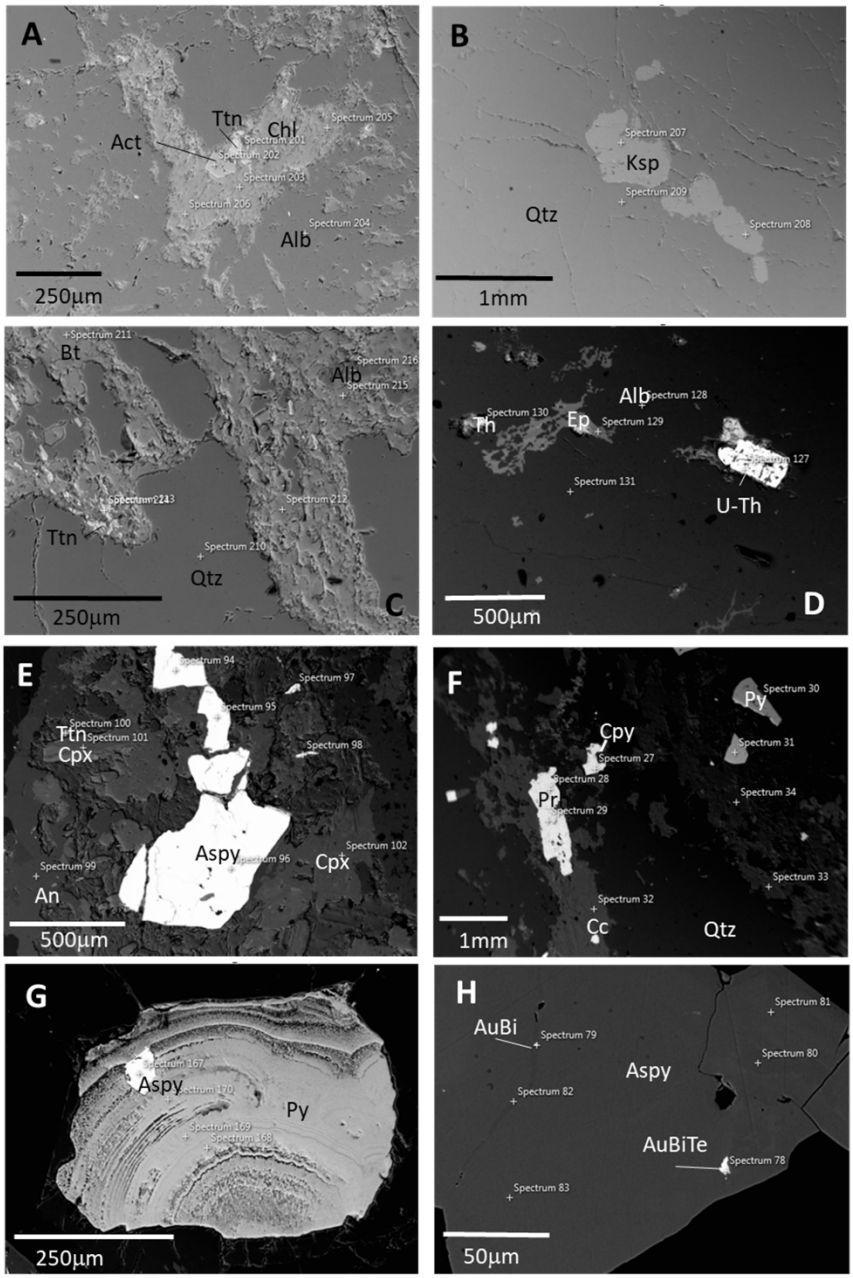

Figure 4: Back scattered electron images of vein petrography from Nalunaq samples. (A) Included wall rock fragment include in main vein (Sample 1). (B) K-feldspar inclusion in main vein quartz (Sample 1). (C) Albite veinlet (D2 extensional vein) cutting main vein quartz (sample 1). (D) Minor mineral inclusions in albite in extensional quartz-feldspar vein (Sample 4) . (E) Arsenopyrite and silicate mineral inclusions in cross-cutting D3 calcite- sulphide vein (Sample 7). (F) Pyrrhotite, chalcopyrite and pyrite in cross-cutting D3 calcite- sulphide vein (Sample 7). (G) Coliform pyrite with arsenopyrite (Sample 5). (H) Maldonite (Au_2Bi) and Au-Bi-Te phase inclusions in arsenopyrite (Sample 3). Act – actinolite; Ttn – titanite; Chl – chlorite; Alb – albite; Qtz – quartz; Ksp – K-feldspar; Bt – biotite; Th – thorianite; Ep – epidote; U-Th – Uranininite/thorianite; Aspy – arsenopyrite; Cpx – clinopyroxene; Pr – pyrrhotite; Cpy – chalcopyrite; Py – pyrite; AuBi – maldonite; Au-Bi-Te – unidentified Au-Bi-Te phase.

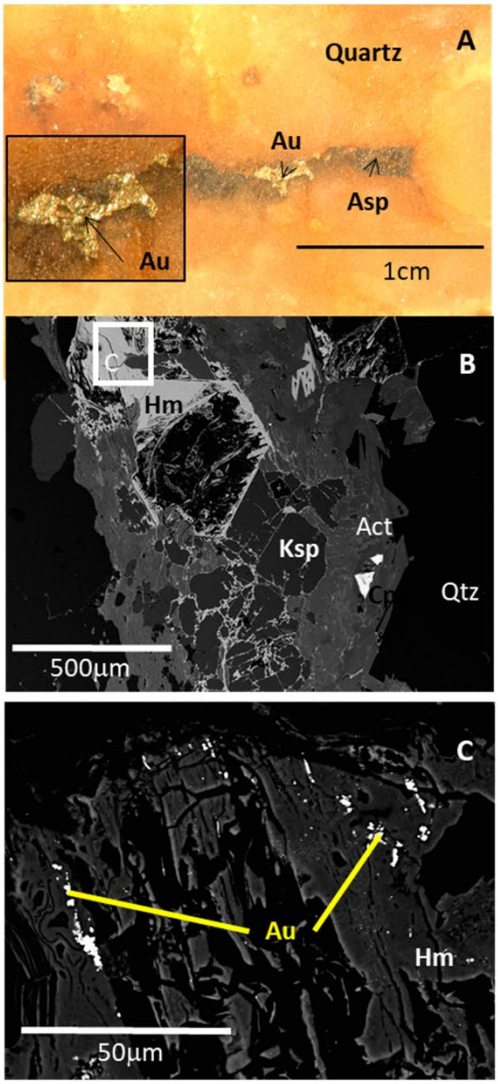

Figure 5: Occurrence of gold associated with arsenopyrite in secondary fractures in quartz. (A) Stereomicroscope image of ~2mm Au grain associated with arsenopyrite. (B) Partially oxidised sulphides associated with actinolite and K-feldspar. Partially weather arsenopyrite is altered to hematite/goethite. (C) High magnification view of iron oxy-hydroxides from B, showing micron scale inclusions of Au. Abbreviations as in Figure 4, with the addition of Hm – hematite.

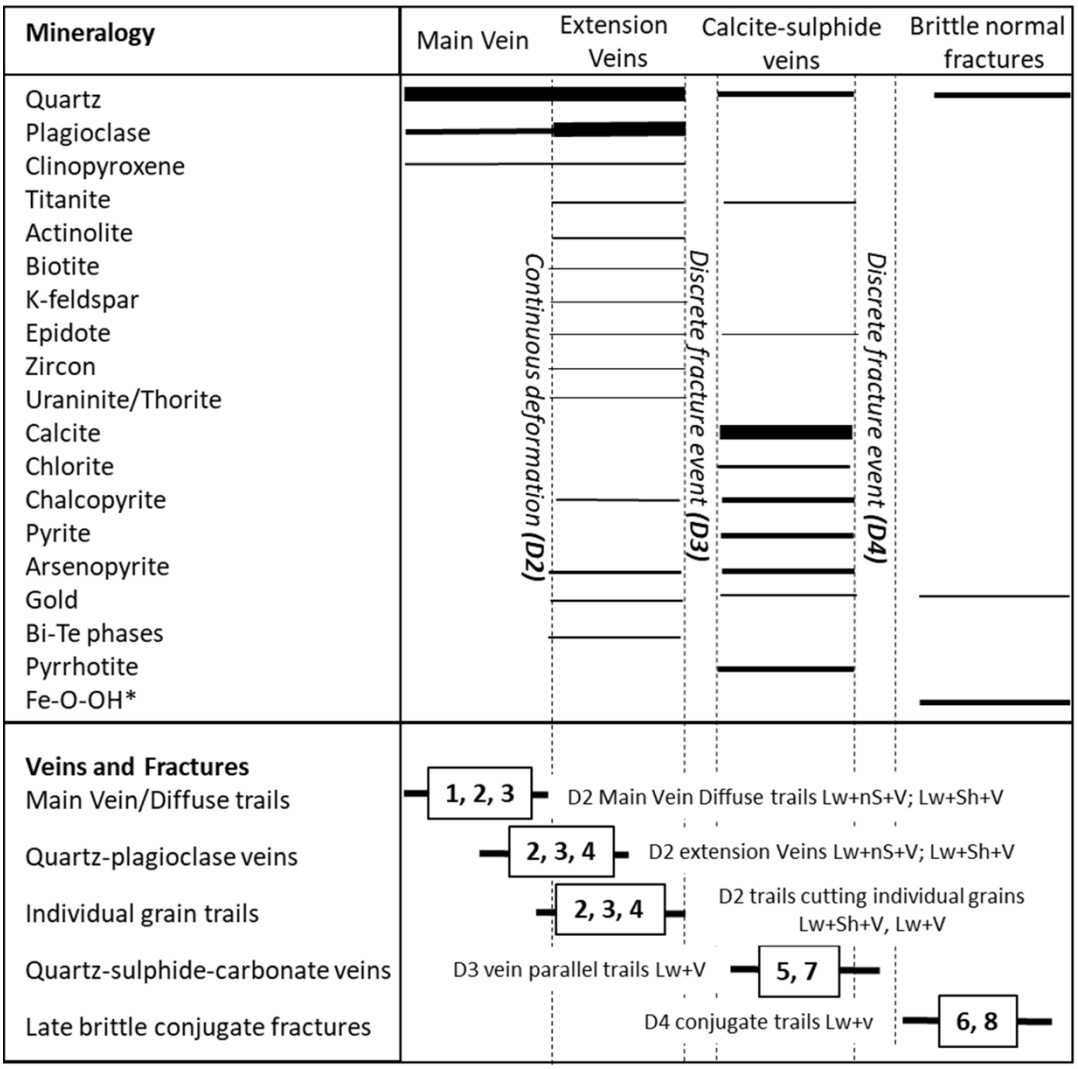

Figure 6: Mineral paragenesis at Nalunaq based on this study and Bell et al., (2017a,b). The vein and fracture paragenesis, and associated fluid inclusion generations are correlated with the deformation events identified by Bell et al., (2017a,.b). Individual fracture groups are labelled with the samples hosting those structures.

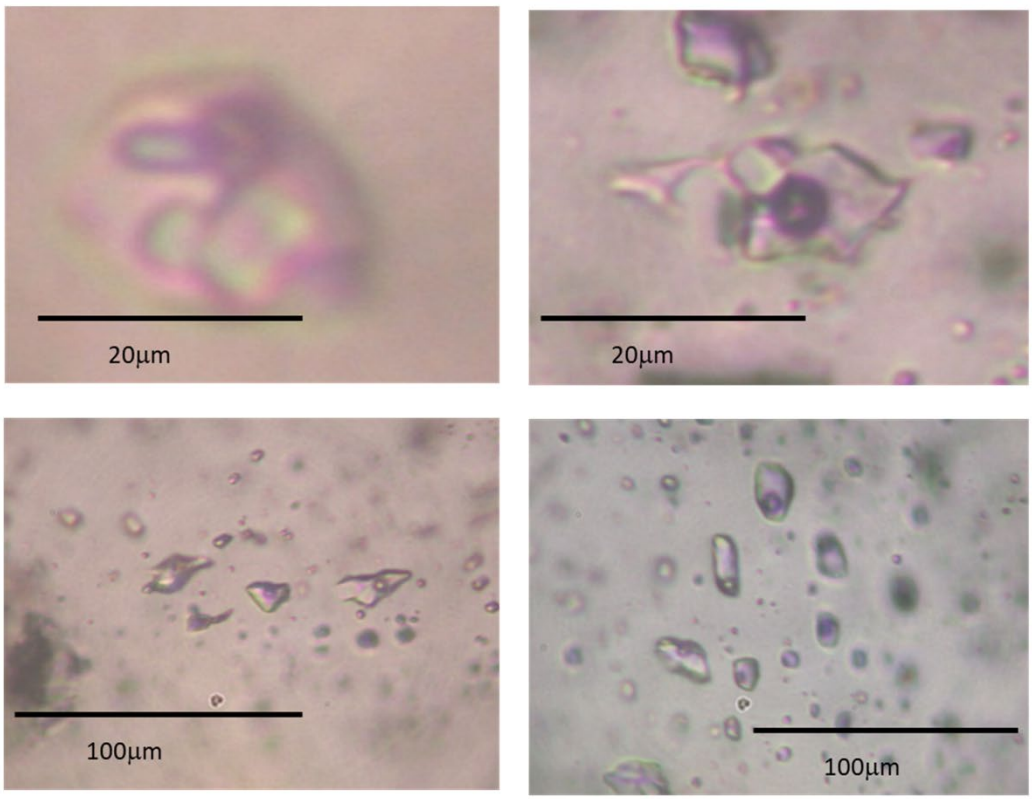

Figure 7: Representative fluid inclusions in quartz. (a) Multisolid (Lw+nS+V) fluid inclusion (population A). (b) Halite-bearing (Lw+Sh+V) inclusion (population B). (C) Aqueous liquid plus vapour (Lw+V) inclusions on secondary trail (Population C). (D) Aqueous liquid plus vapour (Lw+V) inclusions on secondary trail (Population D).

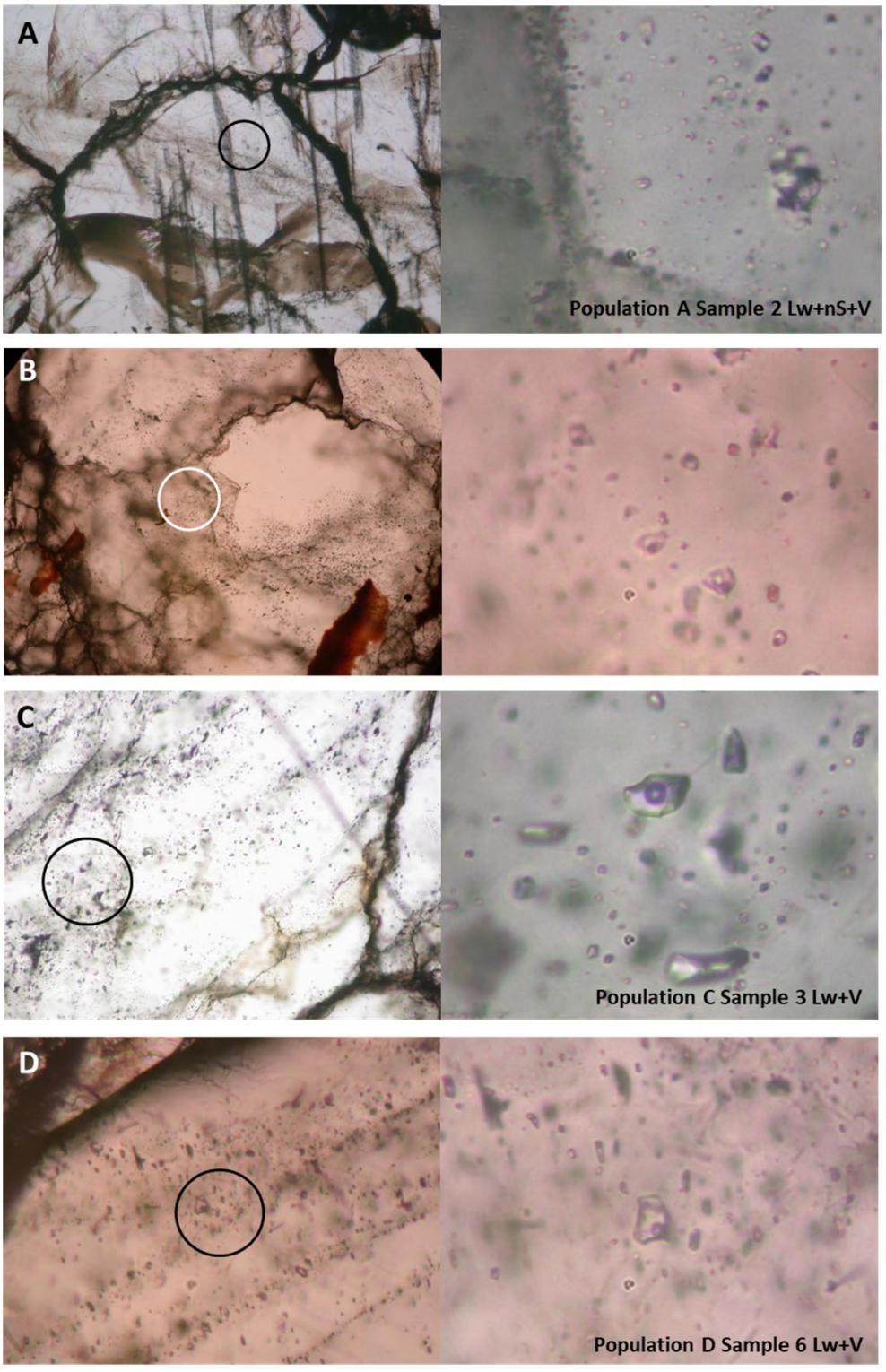

Figure 8: Transmitted light photomicrographs illustrating the structural and petrographic setting of fluid inclusions in quartz. (A) Lw+nS+V inclusion in isolated group restricted to single grain. (B) Lw+Sh+V inclusion in trail restricted to single grain. (C) Lw+V inclusion in trail cutting multiple grains. (D) Lw+V inclusion in conjugate trails cutting multiple grains.

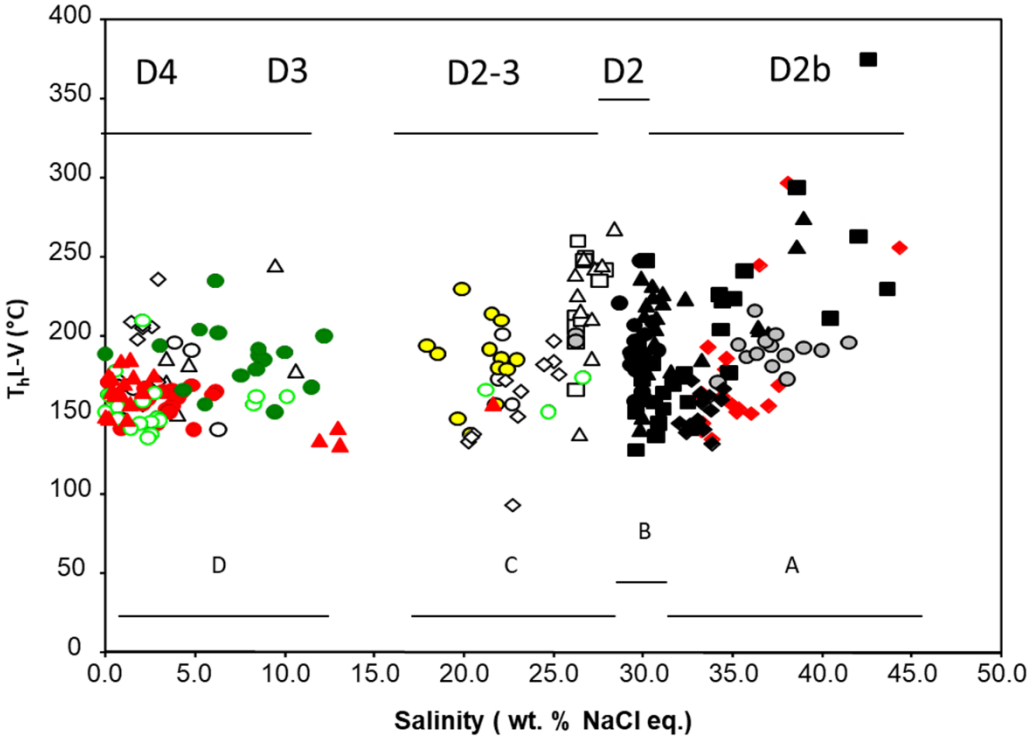

Sample	Inclusions	Sample Au grade
Sample1 ◆	Lw+Sh+V	0.5 g/t
Sample 2 ■	Lw+Sh+V	12.6-18.2 g/t
□	Lw+V	
Sample 3 ▲	Lw+Sh+V	18-25 g/t
△	Lw+V	
Sample 4 ●	Main vein Lw+Sh+V	21-122 g/t
○	Main Vein Lw+V	
●	Feld. veinlet Lw+Sh+V	
●	Feld. veinlet Lw+V	

Sample	Inclusions	Sample Au grade
Sample 5 ◇	Lw+V	2.1 g/t
◆	Lw+Sh+V	
Sample 6 ●	Lw+V	2.6 g/t
Sample 7 ●	cutting vein Lw+V	196.2 g/t
○	Main vein Lw+V	
Sample 8 ▲	Lw+V	0.2 g/t

Figure 9: Fluid inclusion microthermometric data from Nalunaq quartz samples. The key shows the samples and fluid inclusion generations with the associated bulk sample gold grade from each sampling interval.

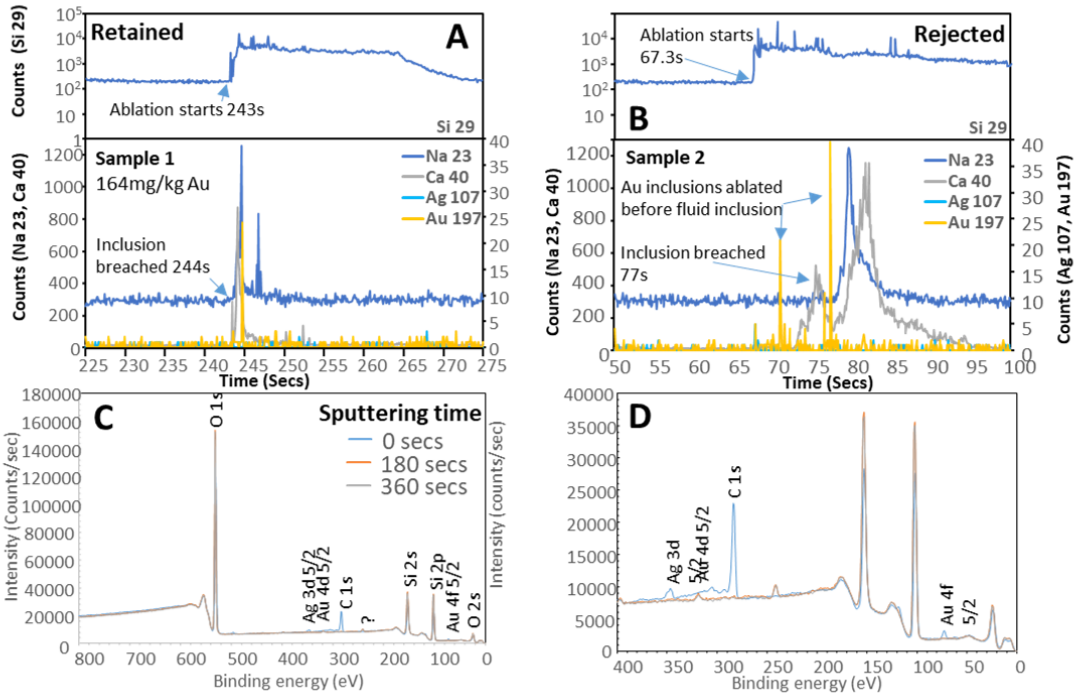

Figure 10: Quality control of fluid inclusion laser ablation ICP-MS analyses. (A) Time resolved mass spectra from fluid inclusion in quartz, showing a good quality. Example of a retained analysis. All mass peaks coincide after the start of ablation, and there are no Au peaks before or after the main inclusion breach. (B) Time resolved mass spectra from fluid inclusion in quartz, showing the influence of Au and mineral microinclusions on the analysis. Example of a rejected analysis. (C) Examples of an XPS binding energy spectrum from quartz. (D) Enlarged plot of the 0-400eV binding energy region from (C). Carbon, Au and Ag are visible as surface contamination before sputtering began. Gold is not detectable in quartz after the removal of the surface layer.

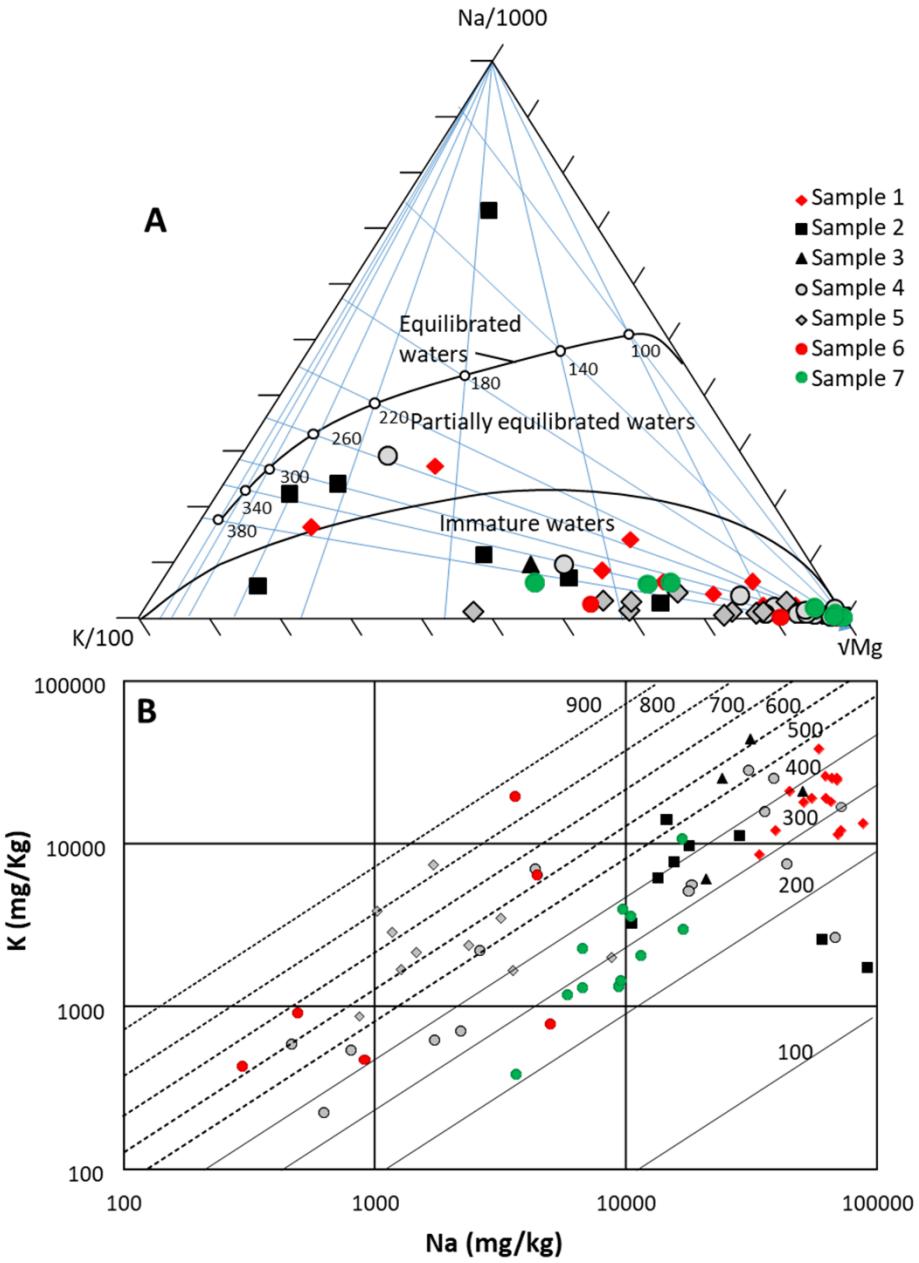

Figure 11: Summary major element chemistry from Nalunaq fluid inclusion LA-ICPMS analyses. (A) Ternary diagram of mole % Na, K and √Mg based on Giggenbach (1988). Equilibration temperature contours were calculated using the Na/K ratio fluid geothermometer of Can (2002) and the K/√Mg ratio fluid geothermometer of Giggenbach (1988). Contours are labelled for the equilibration temperature at their intersection which defines the equilibrated fluids line. The line subdividing partially equilibrated waters from immature waters is from Giggenbach (1988). (B) Plot of K versus Na (mg/kg), contoured for temperature using the equation of Can (2002). Solid lines are calculated within the original calibration range of the equations. Dashed lines are extrapolations beyond the calibration range.

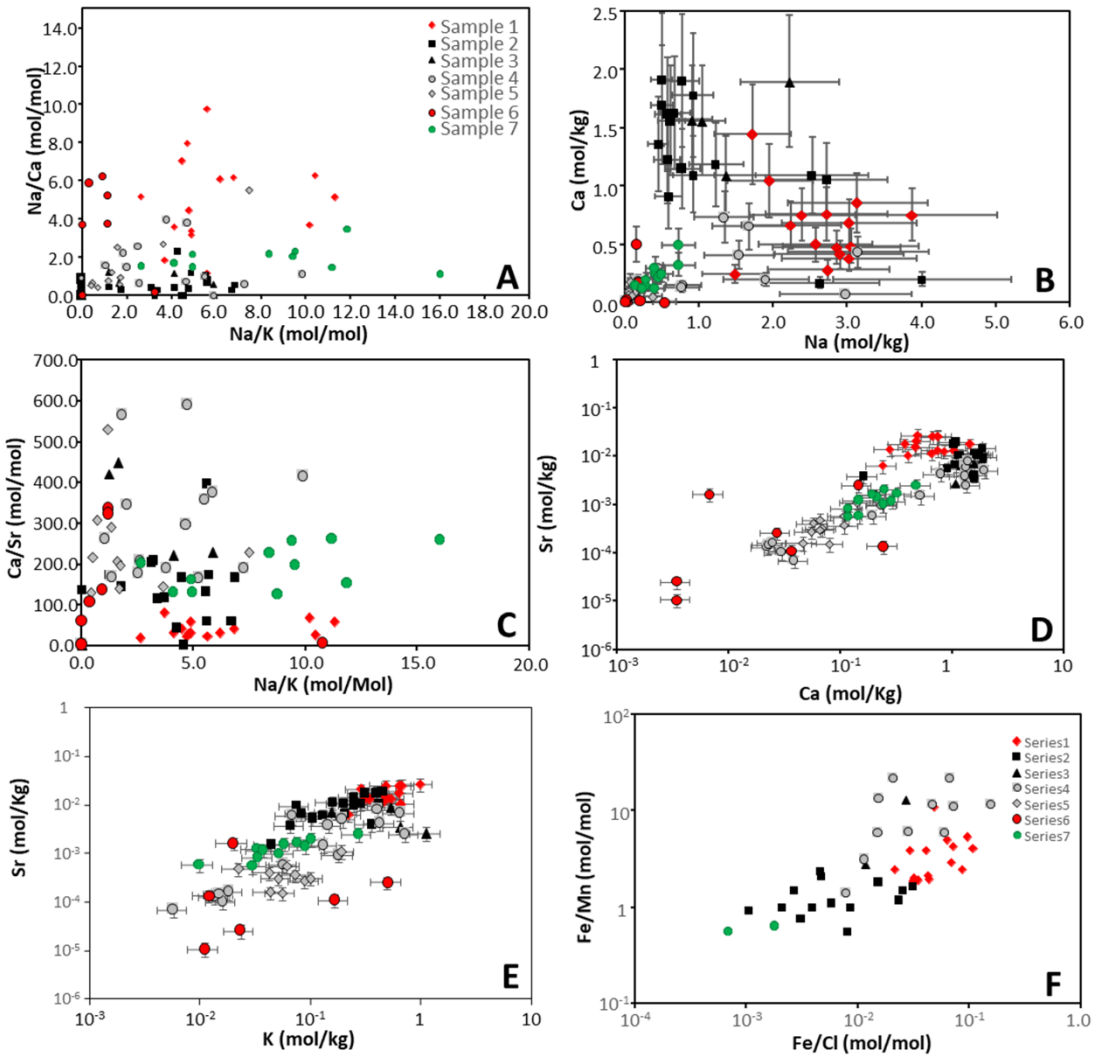

Figure 12: Results of major element chemistry from Nalunaq fluid inclusion LA-ICPMS analyses. (A) Na/K versus Na/Ca ratio. Cooling trend based on the increase in Na/K ratio, mixing trend inferred from range of Na/Ca ratio at fixed Na/K. (B) Na (mol/kg) versus Ca (mol/kg) showing inferred mixing and dilution trends. (C) Na/K versus Ca/Sr showing inferred mixing and cooling trends. (D) Ca (mol/kg) versus Sr (mol/kg) showing inferred mixing and dilution trends. (E) K (mol/kg) versus Sr (mol/kg). (F) Fe/Cl versus Fe/Mn ratio (Yardley, 2005) showing inferred influence of fluid T and oxidation and reduction.

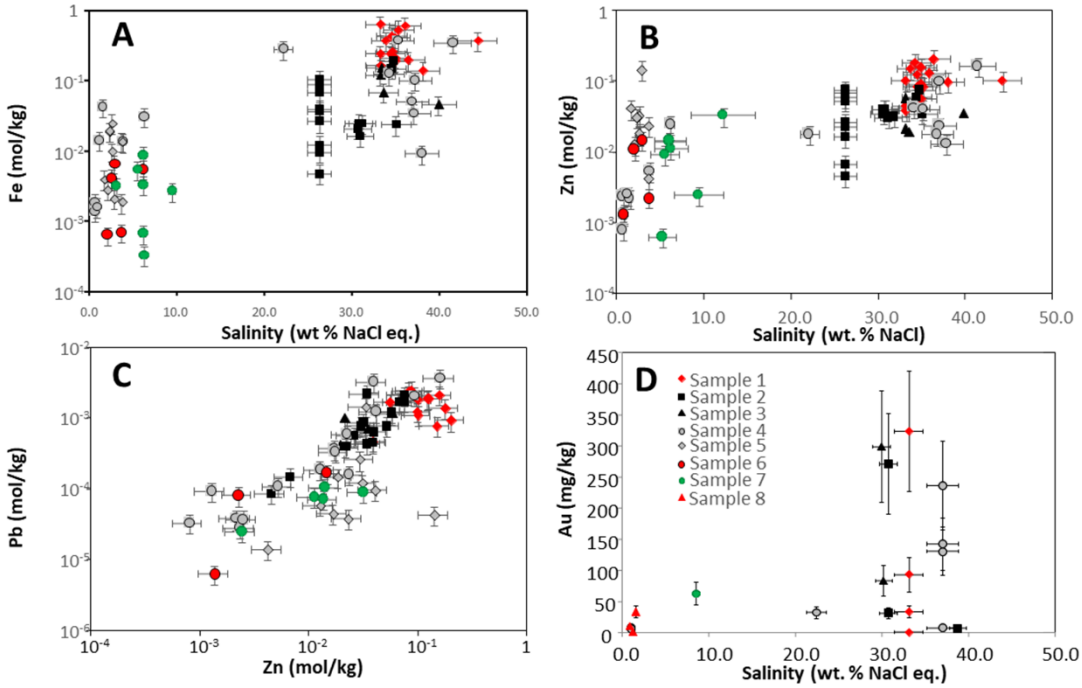

Figure 13: Results of transition metal chemistry from Nalunaq fluid inclusion LA-ICPMS analyses. (A) Fe (mol/kg) versus salinity. (B) Zn (mol/kg) versus salinity. (C) Zn (mol/kg) versus Pb (mol/kg). (c) Au (ppm) versus salinity.

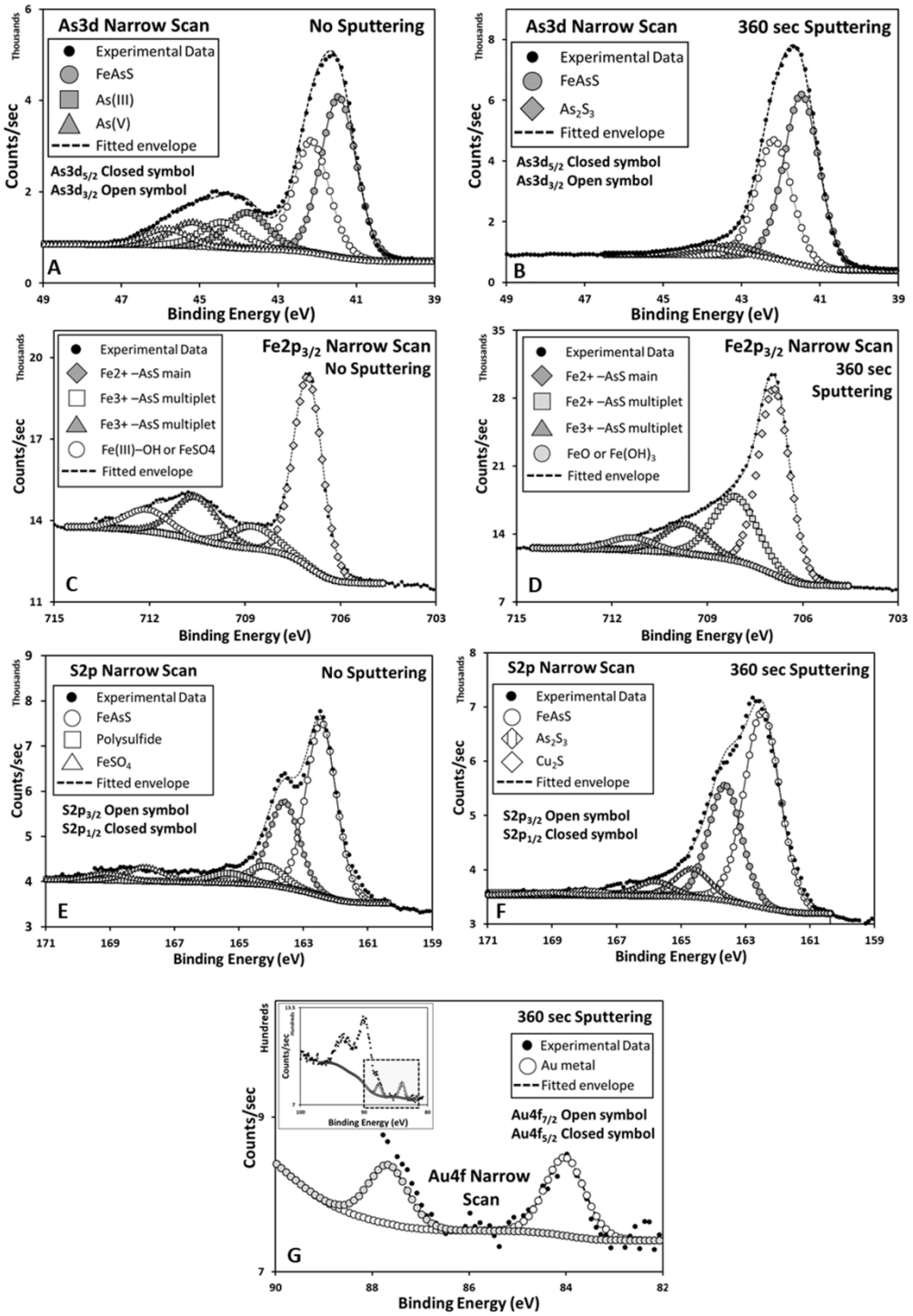

Figure 14: Narrow scans of binding energy spectra from arsenopyrite and associated goethite alteration products. (A) – (F) Analyses of arsenopyrite after no and 360 seconds sputtering with Ar^{+} ion beam. (G) Spectrum of the Au4f binding energy peak in oxidised arsenopyrite. Inset shows the main Fe 3s peak. The Au 4f 5/2 peak is developed as a shoulder on the Fe3s peak.

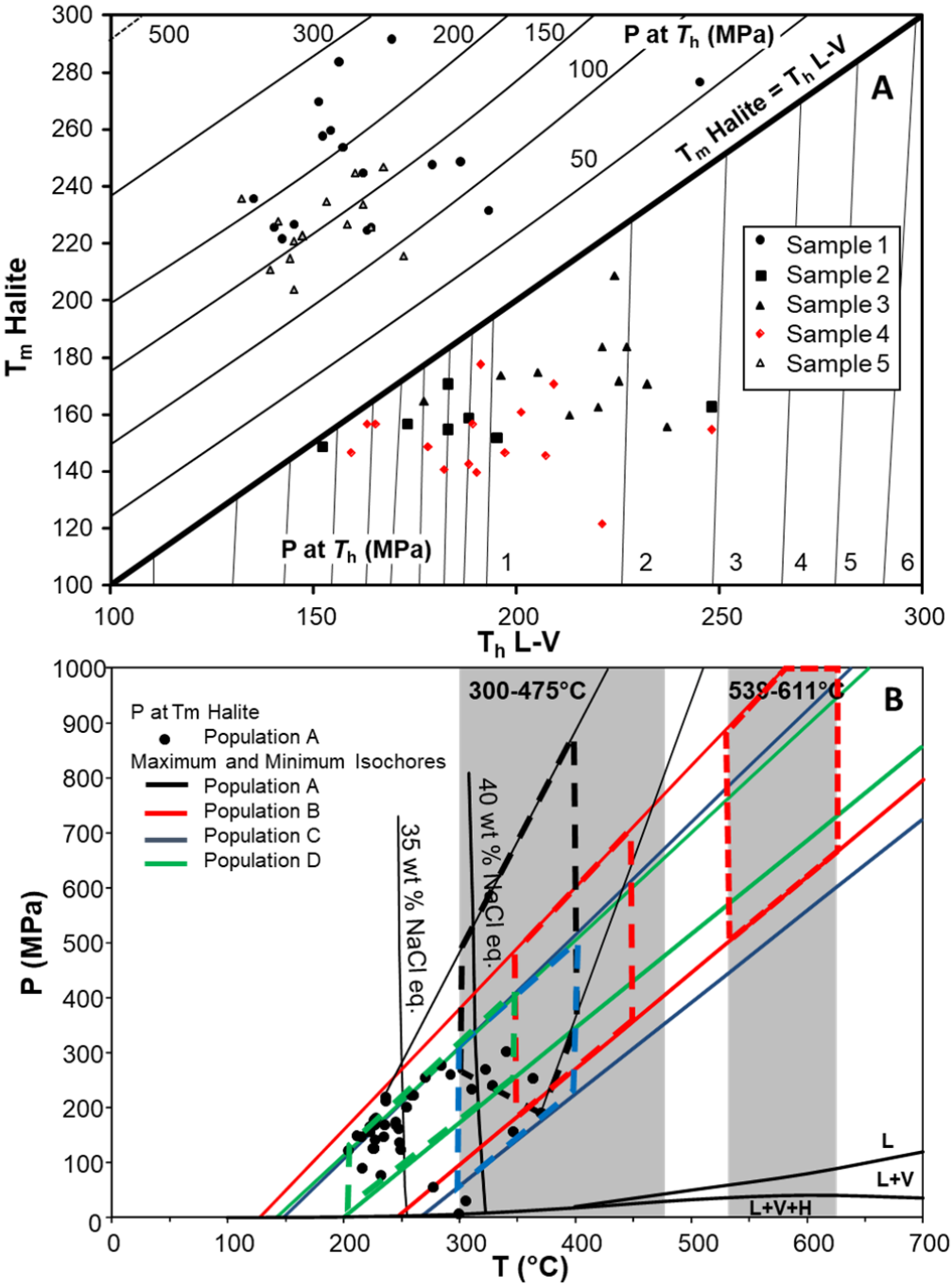

Figure 15 (A) Plot of halite melting temperature against L-V homogenisation temperature. Contours of P and Th calculated from Lecumberri-Sanchez et al. (2012). (B) Estimated range of isochores and P at Th for fluid inclusions. Range of arsenopyrite temperatures from Kaltoft et al. (2000) are shown for comparison. Isochores calculated from Bakker (2003) using the equation of Zhang and Frantz (1987). Halite solidi for different compositions calculated from Becker et al., (2008) and Lecumberri-Sanchez et al. (2012). Phase boundaries from Sourirajan and Kennedy (1962).

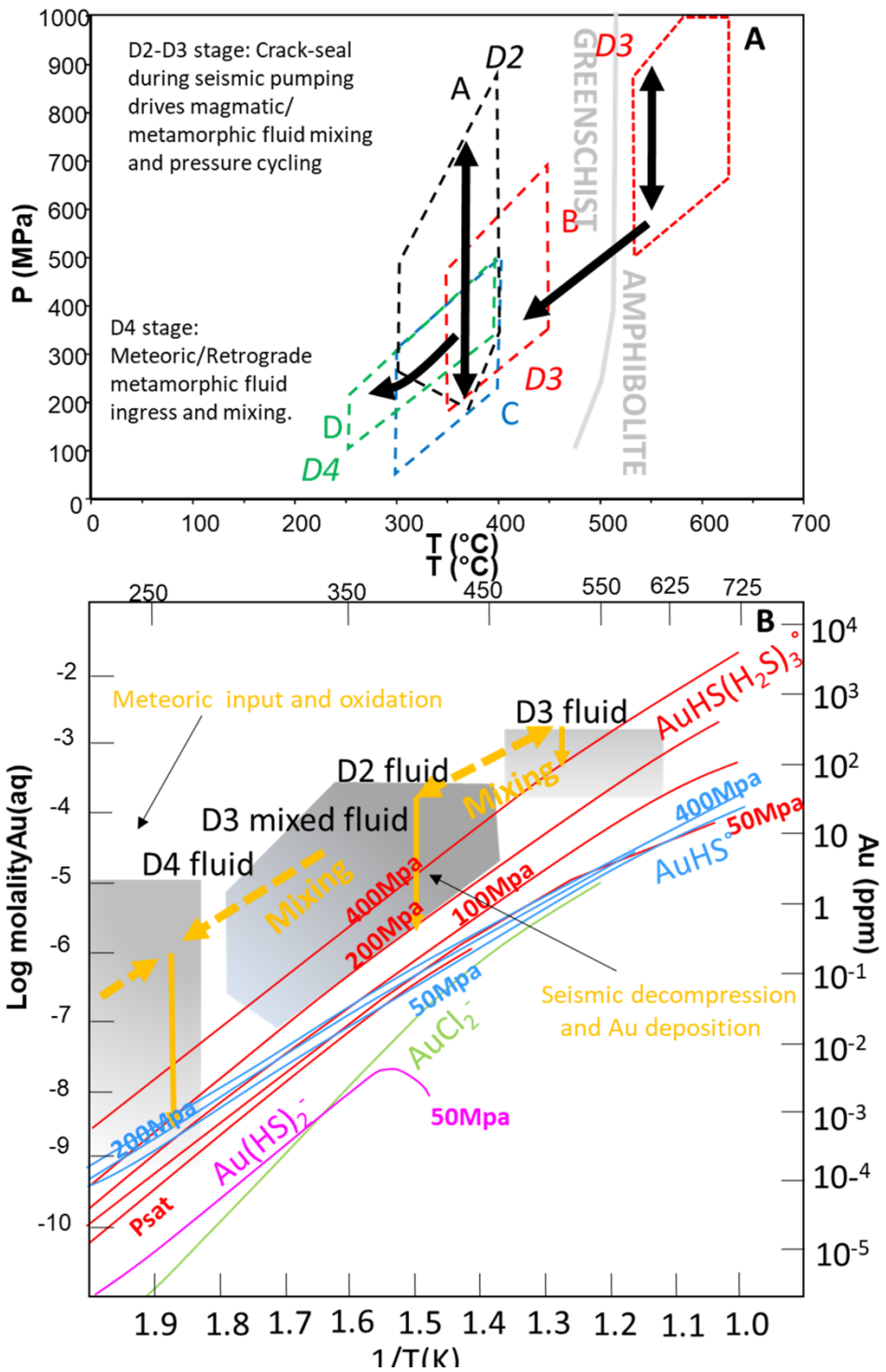

Figure 16: Summary model of fluid evolution and gold solubility and precipitation in Nalunaq fluids. (A) Inferred P-T evolution of Nalunaq veins fluids during deformation. (B) Gold solubility as a range of complex ions (modified from Louks and Mavrogenes, 1999). The extension of the curve for solubility as $AuCl_2^-$ from Williams-Jones et al. (2009). Shaded regions show inferred conditions and Au solubility during evolution of the Nalunaq vein system. Lower limits of Au solubility are below detection limits for the LA-ICPMS method used.

Tables

Sample		Inclusion	N	Tfm	Tm ice		Tm hh		Th L-V		T sol halite		Salinity	
				Mean	Mean	Range	Mean	Range	Mean	Range	Mean	Range	Mean	Range
Sample 1														
	Single grain diffuse trails	Lw+nS+V	19						176	135 - 297	258	222 - 370	35.4	33.0 - 44.3
Sample 2												149 - 363		
	Single grain diffuse trails/plagiolcase veinlets	Lw+Sh+V	29						196	128 - 375	220	16.5 - 97	33.5	29.6 - 43.6
	Individual grain planar trails	Lw+V	6	-65	-36.8	-36 - 37.6	9	6 - 11	241	210 - 260	54		27.0	26.4 - 27.9
	Individual grain planar trails	Lw+V	4	-45	-5.8	-5.1 - -6.1			195	166 - 212			8.9	8.0 - 9.3
Sample 3														
	Individual grain planar trails	Lw+Sh+V	22						206	141 - 275	202	155 - 310	32.3	30 - 38.9
	Quartz-carbonate veinlet	Lw+V	13	-66	-39.36	-35.8 - -47	-15.6	-13.9 - -17.3	222	138 - 268	50.5	2.4 - 114	26.9	26.3 - 28.4
	Individual grain planar trails	Lw+V	6	-43	-3.8	-2.0 - -7.1			186	151 - 245			5.9	3.4 - 10.6
Sample 4 Main vein														
	Individual grain planar and diffuse trails	Lw+Sh+V	16						193	159 -248	150	122 - 178	29.7	28.7 - 30.8
	Cross-cutting conjugate trails	Lw+V	8	-52.1	-1.5	-0.4 - -2.9			169	141 - 191			2.5	0.7 - 4.8
	Individual grain planar and diffuse trails	Lw+V	3	-55.3	-19.4	-19 - -20	-31.3	-29.3 - -39.7	177	157 - 201			22.3	21.9 - 22.7
Sample 4 Cross cutting quartz-feldspar vein														
	Individual grain planar and diffuse trails	Lw+nS+V	16						192	171 - 216	288	242 - 340	35.9	34.2 - 41.5
	Individual grain planar and diffuse trails	Lw+V	13	-61	-17.8	-14.0 - -20.4	-39	-37.0 - -45.0	185	138 - 230			20.9	17.9 - 22.9
Sample 5														
	Cross-cutting conjugate trails	Lw+V	9	-55	-1.4	-0.8 - -2.2			194	156 - 236			2.4	1.4 - 3.7
	Quartz-carbonate vein parallel trails	Lw+V	11	-64	-20.5	-17.0 - -24.0	-40	-35 - -46.5	157	93 - 197			22.9	20.3 - 25.4
	Individual grain planar and diffuse trails	Lw+Sh+V	15						152	132 - 172	226	204 - 247	33.3	32.1 - 34.5
Sample 6														
	Cross-cutting conjugate trails	Lw+V	21	-24.6	-1.9	-0.1 - -3.8			158	142 - 171			3.1	0.2 - 6.1
Sample 7 main vein														
	Individual grain planar trails	Lw+V	4	-63	-18.4	-6.7 - -26.0	-43		164	152 - 174			20.6	10.1 - 26.6
	Cross-cutting conjugate trails	Lw+V	18	-42	-1.4	0 - -5.4			156	136 - 210			2.4	0 - 8.3
Sample 7 Cross cutting calcite-sulphide vein														
	Quartz-carbonate vein parallel trails	Lw+V	16	-43.2	-4.6	-1.8 - -8.4			186	152 - 235			7.2	3.1 - 12.2
Sample 8														
	Cross-cutting conjugate trails	Lw+V	14	-20	-0.5	-0.1 - -1.2			167	148 - 185			0.9	0.2 - 2.1
	Planar trails	Lw+V	6	-56.8	-11.3	-8.2 - -18.6	-37.7	-36.8 - -39.3	143	131 - 157			14.9	12.0 - 21.6

Table 1: Summary of Microthermometric data from Nalunaq quartz-hosted fluid inclusions. See text for abbreviation defintions.

Analysis no.		NAL-1B	Nal-1d	Nal1Bi	NAL1Bii	NAL-2B	NAL2Ai	NAL-3A	NAL3CI	NAL-4C	NAL-4E	NAL4Dii	NAL4Ei	NAL-5A	NAL-6A	NAL-7B	NAL-7B	NAL7Ai	NAL8ai
salinity		33.20	44.32	33.09	33.09	26.24	30.70	33.31	30.18	41.49	6.29	36.97	1.05	2.40	3.69	12.19	6.29	8.54	0.87
Cl molality		5.67	7.58	5.66	5.66	4.49	5.25	5.69	5.16	7.09	1.07	6.32	0.18	0.41	0.63	2.08	1.07	1.46	0.15
Raw data normalised to 1 ug/g Na																			
Na23	µg/g	1	1	1.00	1.00	1	1.00	1	1.00	1	1	1.00	1.00	1	1	1	1	1.00	1.00
Mg24	µg/g	0.085	0.523			0.016		0.639		0.319	0.264			0.371	1.122	0.017	0.023		
K39	µg/g	0.275	0.304			0.499		0.290		0.655	1.616			3.788	0.521	0.638	0.412		
Ca40	µg/g	0.286	0.178	1.42	0.47	4.165	6.38	2.991	2.12	1.356	2.198	0.95	1.74	2.548	10.733	1.156	1.029	0.28	1.35
Mn55	µg/g	0.095	0.030			0.134		0.032		0.043	0.065			<0.0550	<0.0496	<0.0106	<0.0039		
Fe56	µg/g	0.206	0.325			0.249		0.413		0.493	0.393			1.043	0.043	0.018	0.018		
Cu63	µg/g	<0.0122	<0.0558			<0.0480		<0.0529		<0.0323	0.093			0.205	<0.1702	<0.032848	0.012		
Zn66	µg/g	0.035	0.037			0.076		0.024		0.096	0.125			0.691	0.057	0.044	0.026		
Sr88	µg/g	0.020	0.019			0.061		0.029		0.015	0.019			0.026	0.013	0.013	0.018		
Ag107	µg/g	0.001	<0.0038			0.057		<0.0022		0.006	<0.0010			<0.0063	0.020	0.023	0.002		
Ba137	µg/g	0.007	0.007			0.010		0.010		0.008	0.013			0.024	<0.0045	0.003	0.004		
Pb208	µg/g	0.003	0.006			0.010		0.010		0.019	0.007			0.024	0.018	0.001	0.002		
Ag107	µg/g			<0.0012	<0.0041		<0.0025		0.001			<0.0004	<0.0003					0.002	<0.0014
Au197	µg/g			0.001	0.004		0.002		0.002			0.002	0.006					0.002	0.007
Reconstructed analyses																			
Na23	mg/kg	65704	63004	49493.3	84384.5	15554	14475.4	20894	34475.5	38793	4367	69320.8	1370.5	1022	910	16794	9695	25485.0	1348.9
Mg24	mg/kg	5582	32948			252		13345		12380	1153			380	1020	279	221		
K39	mg/kg	18067	19135			7763		6050		25424	7055			3873	474	10718	3991		
Ca40	mg/kg	18765	11245	70074.7	39705.0	64777	92358.9	62503	73195.2	52618	9598	66098.7	2385.6	2605	9763	19414	9980	7012.4	1815.0
Mn55	mg/kg	6246	1859			2083		659		1653	283								
Fe56	mg/kg	13547	20499			3869		8620		19110	1717			1066	40	302	179		
Cu63	mg/kg										388			200					
Zn66	mg/kg	6632	6657			3405		1409		10636	1564			2027	149	2117	736		
Sr88	mg/kg	1341	1204			943		604		568	82			27	12	215	171		
Ag107	mg/kg	34				892				222					18	390	20		
Ba137	mg/kg	457	421			152		205		293	56			25		43	42		
Pb208	mg/kg	225	375			162		213		754	32			25	17	19	16		
Ag107	mg/kg			0.00	0.00		0.00		35.23			0.00	0.00					61.39	0.00
Au197	mg/kg			33.0	323.1		30.4		82.5			129.7	7.7					61.9	9.5

Table 2: Representative results of LA-ICPMS analysis of fluid inclusions. All data have been filtered for detection limits and the presence of gold micro- and nano-inclusion in quartz. Concentrations reconstructed using the method of Allan et al., (2005).

Supplementary Tables.

Table S1: Full fluid inclusion microthermometric data set from Nalunaq quartz.

Table S2: Full LA-ICPMS data set for the extended element list analyses. Salinities determined from microthermometric analyses, and used to calculate chlorinity. Concentrations reconstructed using the method of Allan et al., (2005).

Table S3: Full LA-ICPMS data set for the Au specific element list analyses. Salinities determined from microthermometric analyses, and used to calculate chlorinity. Concentrations reconstructed using the method of Allan et al., (2005).